nature communications

Article

https://doi.org/10.1038/s41467-025-61552-0

EMP1 safeguards hematopoietic stem cells by suppressing sphingolipid metabolism and alleviating endoplasmic reticulum stress

Received: 5 October 2024

Accepted: 20 June 2025

Published online: 07 July 2025

Check for updates

Lei Li[1,9], Yufei Lei[2,9], Yan Li[3,9], Yuxin Xie[2], Pusheng Hui[4], Xiaoyan Zang[5], Weiru Wu[6], Feng Wu[2], Jiankun Fan[2], Jianming Wang[2], Jieping Chen[1,7] ✉, Zhe Chen[2,8] ✉ & Yu Hou[2,8] ✉

The long-term maintenance of hematopoietic stem cells (HSCs) relies on the regulation of endoplasmic reticulum (ER) stress at a low level, but the underlying mechanism remains poorly understood. Here, we demonstrate that suppression of ER stress improves the functions of HSCs and protects HSCs against ionizing radiation (IR)-induced injury. We identify epithelial membrane protein 1 (EMP1) as a key regulator that mitigates ER stress in HSCs. *Emp1* deficiency leads to the accumulation of protein aggregates and elevated ER stress, ultimately resulting in impaired HSC maintenance and self-renewal. Mechanistically, EMP1 is located within the ER and interacts with ceramide synthase 2 (CERS2) to limit the production of a class of sphingolipids, dihydroceramides (dhCers). DhCers accumulate in *Emp1*-deficient HSCs and induce protein aggregation. Furthermore, *Emp1* deficiency renders HSCs more susceptible to IR, while overexpression of *Emp1* or inhibition of CERS2 protects HSCs against IR-induced injury. These findings highlight the critical role played by the EMP1-CERS2-dhCers axis in constraining ER stress and preserving HSC potential.

The blood system is sustained by a pool of hematopoietic stem cells (HSCs) that are responsible for the production of all blood lineages[1,2]. HSCs possess the capacity for self-renewal to ensure their long-term maintenance. Consequently, HSCs are exposed to multiple stress stimuli, including nutrient fluctuation, reactive oxygen species (ROS), endoplasmic reticulum (ER) stress, DNA damage, and replication stress[3–7]. The molecular regulatory networks in HSCs tightly control stress-induced damage to prevent loss of function or the risk of leukemogenesis[8]. However, there still exist major gaps in understanding how HSCs respond to stress, which hinders the development of strategies to maintain or expand functional HSCs in vivo.

ER is the largest organelle in eukaryotic cells and is responsible for various important cellular functions[9]. Various stimuli can lead to the accumulation of unfolded and misfolded proteins, which is a major cause of ER stress[10]. The response to ER stress, also known as the unfolded protein response (UPR), involves multiple reactions aimed at restoring protein folding homeostasis by reducing protein synthesis and improving the capacity of the ER for protein folding and degradation. If ER stress cannot be relieved, proapoptotic signaling will be

[1]College of Bioengineering, Chongqing University, Chongqing, China. [2]School of Basic Medical Sciences, Chongqing Medical University, Chongqing, China. [3]Department of Neurology, Xinqiao Hospital and The Second Affiliated Hospital, Third Military Medical University (Army Medical University), Chongqing, China. [4]Department of Urology, The First Affiliated Hospital of Chongqing Medical University, Chongqing, China. [5]Department of Hematology, The First Affiliated Hospital of Chongqing Medical University, Chongqing, China. [6]Department of Clinical Hematology, Third Military Medical University (Army Medical University), Chongqing, China. [7]Department of Hematology, Southwest Hospital, Third Military Medical University (Army Medical University), Chongqing, China. [8]Chongqing Key Laboratory of Hematology and Microenvironment, Chongqing, China. [9]These authors contributed equally: Lei Li, Yufei Lei, Yan Li. ✉e-mail: chenjpxn@163.com; chenzhe925@cqmu.edu.cn; houyu@cqmu.edu.cn

initiated to clear the damaged cells[11]. Human HSCs are susceptible to ER stress and initiate apoptosis relative to other hematopoietic progenitors[5,12,13]. Enhanced ER protein folding significantly improves the reconstitution capacity of HSCs. By contrast, the deletion of the most conserved UPR transducer inositol-requiring enzyme 1α (IRE1α) impairs it[5,12]. It has been demonstrated that IRE1α safeguards HSCs by restricting pro-leukemogenic gene programs[14]. Moreover, suppression of protein aggregation and ER stress by bile acids is necessary for promoting HSC proliferation during fetal hematopoiesis[15]. These findings indicate that HSCs require restricted levels of ER stress for their long-term maintenance; however, the mechanisms by which HSCs regulate or constrain this level of ER stress remain poorly understood.

Epithelial membrane protein 1 (EMP1) is an integral membrane glycoprotein and belongs to the peripheral myelin protein 22-kDa (PMP22) gene family[16]. *EMP1* has been identified as an oncogene in multiple cancers, including leukemia[16,17]. High expression of *EMP1* has been observed in prednisolone-resistant patients compared to -sensitive patients. Additionally, knock-down of *EMP1* significantly reduces the migration capacity of acute lymphoblastic leukemia (ALL) cell lines. Furthermore, EMP1 has been recognized as a prognostic factor in myelodysplastic syndrome (MDS) and acute myeloid leukemia (AML)[18,19], and it is also considered a stemness-related gene in leukemia stem cells (LSCs)[20]. These findings underscore the critical roles of EMP1 in hematologic disorders; however, its exact functions in normal hematopoiesis, particularly in HSCs, remain unknown.

In this study, we confirmed the susceptibility of HSCs to ER stress. We observed that suppression of ER stress enhances HSC maintenance and repopulation capacity both in vitro and in vivo while also providing protection against ionizing radiation (IR)-induced injury. Moreover, we have identified a gene, *EMP1*, that constrains ER stress in HSCs under homeostatic or IR conditions. Loss of *Emp1* impairs HSC maintenance and self-renewal. The ER-localized EMP1 binds ceramide synthase 2 (CERS2) to constrain the production of dihydroceramides, thereby preventing the formation of protein aggregation within HSCs. Our findings emphasize the crucial role of EMP1 in preserving HSC potential and reveal a link between sphingolipid metabolism and HSC homeostasis.

Results

Suppression of ER stress contributes to the preservation of HSC potential

It has been demonstrated that human HSCs exhibit a higher sensitivity to ER stress compared to progenitor cells in vitro, as evidenced by more pronounced apoptosis[5]. To investigate the sensitivity of HSCs to ER stress in vivo, *wild-type* C57BL/6J mice were treated with tunicamycin (2 mg/kg) (Fig. S1A), an inhibitor of glycosylation to disturb the protein folding[21]. The fluorogenic assay utilizing the ProteoStat dye has been developed to monitor protein aggregation within cells[15] (Fig. S1B). Twenty-four hours after the administration of tunicamycin, we performed ProteoStat dye staining and observed the significant increase in aggregated protein levels in bone marrow (BM) HSCs (Fig. S1C), which are usually characterized as $CD48^-CD150^+$LSK (LSK refers to $Lineage^-Sca\text{-}1^+c\text{-}kit^+$ cells)[22]. This increase was most pronounced in HSCs compared to other hematopoietic cell types (Fig. S1C). The accumulation of unfolded/aggregated proteins triggers UPR, which is regulated by three branches: the PRKR-like ER kinase (PERK), inositol-requiring enzyme 1 (IRE1), and activating transcription factor (ATF6)[11]. Our observations indicated that the UPR response of HSCs to tunicamycin treatment was more robust compared to LK cells ($Lin^-Sca\text{-}1^-c\text{-}kit^+$ cells; Lin^- refers to $lineage^-$ cells) and LSK cells, as evidenced by increased phosphorylation of IRE1 and PERK (Fig. S1D, E). These data suggest that HSCs are susceptible to ER stress in vivo.

To further investigate the impact of ER stress on HSC maintenance in vitro, we cultured BM Lin^- cells from *wild-type* mice in a liquid medium. The cultures were treated with either dimethyl sulfoxide (DMSO), tunicamycin (5 μM) to induce ER stress, or azoramide (15 μM) to enhance ER protein folding and increase chaperone activity for a duration of 24 h (Fig. 1A). Compared to the DMSO-treated culture samples, those treated with tunicamycin exhibited a reduced frequency of LSK and HSCs among the cultured cells; however, treatment with azoramide appeared to mitigate this effect and even promote the preservation of HSCs when compared to the DMSO group (0.049% versus 0.025%) (Fig. 1B). We also cultured sorted HSCs ($CD48^-CD150^+$LSK) under the same conditions, followed by a serial colony-forming unit (CFU) assay. Our findings indicated that tunicamycin significantly inhibited the colony-forming capacity of HSCs. In contrast, the suppression of ER stress through azoramide substantially enhanced the number of CFUs generated by HSCs (Fig. 1C).

Competitive BM transplantation is enabled by antibodies that specifically recognize hematopoietic cells from congenic mouse strains due to variants of the cell surface protein CD45, designated CD45.1 and CD45.2. The C57BL/6J background mice express the CD45.2 allele, whereas B6.SJL mice express the CD45.1 allele. Offspring resulting from the crossbreeding of these two mouse strains simultaneously express both CD45.1 and CD45.2 alleles[23]. To further assess the reconstitution potential of HSCs in vivo, drug-treated HSCs (CD45.2) derived from *wild-type* C57BL/6J mice were mixed with competitor BM cells (CD45.1) and transplanted into lethally irradiated recipient mice (CD45.1CD45.2). Our findings indicate that treatment with azoramide or tunicamycin resulted in the highest and lowest chimeric percentages of donor-derived peripheral blood (PB), respectively (Fig. 1D, E). The chimeric percentages of mature cells, including myeloid, B, and T cells in PB, exhibited a consistent change at 4 months post-transplantation (Fig. S1F). Furthermore, azoramide or tunicamycin treatment led to the highest and lowest chimeric percentages observed in BM cells, LK cells, LSK cells, and HSCs within recipient mice, respectively (Fig. 1F). Taken together, these data suggest that suppression of ER stress improves both in vitro maintenance and in vivo repopulation potential for HSCs.

Alleviation of ER stress protects HSCs against radiation-induced injury

IR is known to cause hematopoietic toxicity, leading to severe consequences such as BM failure, immune dysfunction, and even leukemia/lymphoma development[24]. HSCs are highly susceptible to IR, which causes HSC dysfunction[25,26]. However, effective strategies for protecting HSCs from IR-induced injury are currently limited. A dosage of 2–5 Gy is commonly utilized for evaluating the impact of IR on HSCs, both in vivo and in vitro[27–29]. To investigate the impact of IR on HSCs in vitro, HSCs ($CD48^-CD150^+$LSK) were isolated from *wild-type* C57BL/6J mice and then exposed to a dose of 2 Gy of γ-irradiation (Fig. S2A). Subsequent analyses at various time points post-irradiation (6–72 h) revealed that 6 h after exposure, the levels of aggregated proteins in HSCs were significantly upregulated, peaking at 24 h and then decreasing dramatically; however, these levels remained elevated compared to non-IR-treated HSCs (Fig. S2B). Additionally, key markers of the UPR, specifically p-IRE1 and p-PERK, exhibited significant elevation in IR-treated HSCs relative to control groups, with peak expression observed at 24 h post-exposure (Fig. S2C). To further explore the effect of IR on HSCs in vivo, *wild-type* C57BL/6J mice were exposed to sublethal doses (2 or 5 Gy) of γ-irradiation (Fig. 1G). Twenty-four hours after exposure, the number of LK, LSK, and HSCs in IR-treated mice was significantly reduced compared to non-IR-treated counterparts (Fig. S2D, E). Consistent with previous findings[24], we observed that IR caused substantial DNA damage in HSCs, as indicated by increased levels of γ-H2AX (Fig. S2F, G). Notably, IR resulted in a significant increase in aggregated protein levels in HSCs (Fig. 1H). The hallmarks of UPR, p-IRE1 and p-PERK, were also remarkably elevated in IR-treated HSCs compared to control HSCs (Fig. 1I). Collectively, these data suggest that IR induces the formation of protein aggregates and elicits ER stress in HSCs both in vitro and in vivo.

To investigate whether the alleviation of ER stress could protect HSCs from IR exposure, murine HSCs ($CD48^-CD150^+$LSK) were treated

https://doi.org/10.1038/s41467-025-61552-0

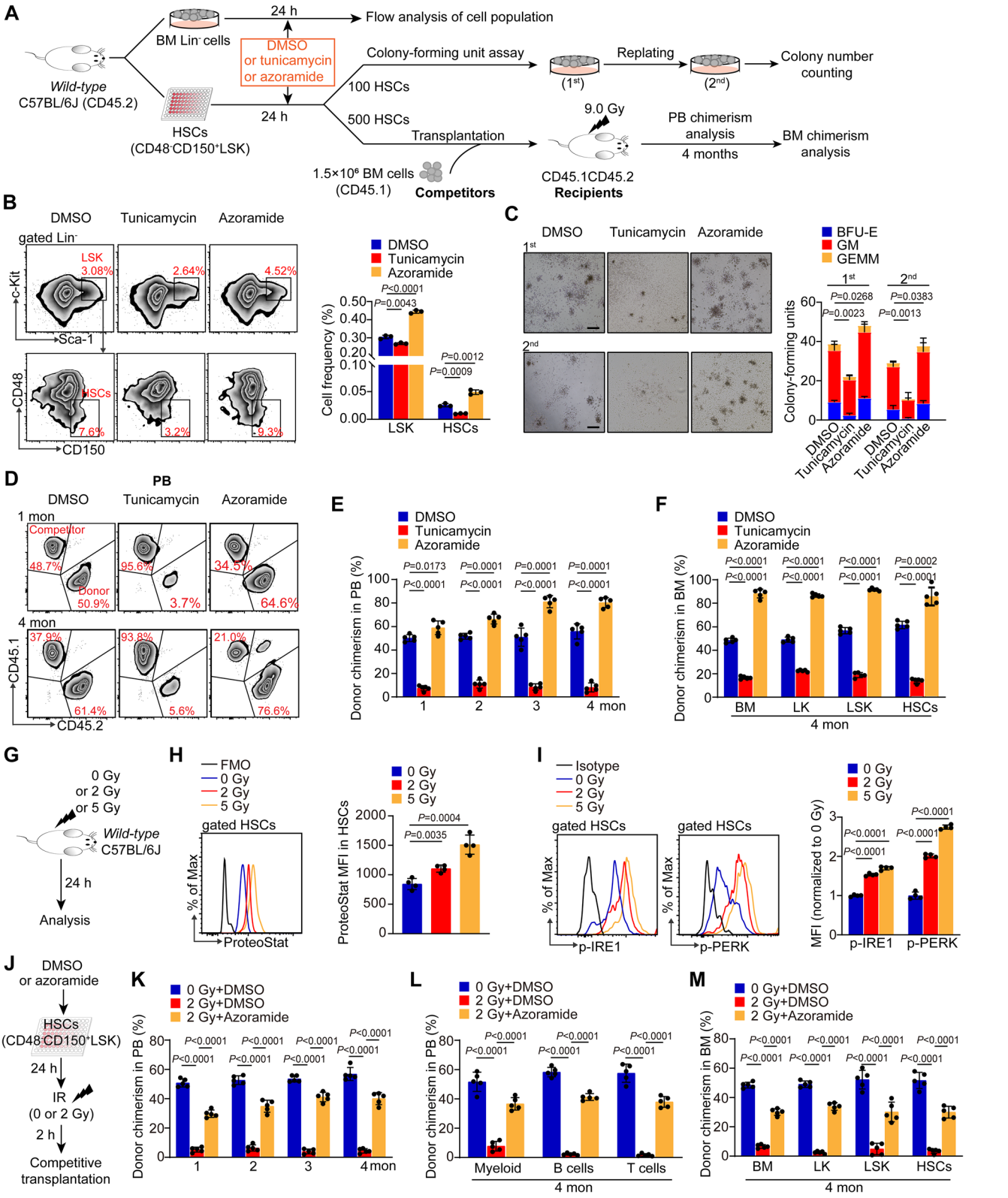

with azoramide to enhance ER protein folding and increase the activity of ER chaperones. Subsequently, the HSCs were exposed to IR at a dose of 2 Gy and then transplanted into recipient mice (Fig. 1J). It was observed that IR treatment significantly decreased the chimeric percentages of donor-derived PB, BM cells, LK, LSK, and HSCs in recipient mice compared to non-IR-treated group. Encouragingly, azoramide treatment markedly enhanced the reconstitution capacity of HSCs in recipient mice (Fig. 1k–m). These findings collectively demonstrate that ER stress plays a pivotal role in IR-induced injury in HSCs, while alleviating ER stress effectively improves HSC function under IR conditions.

ER stress induces the expression of EMP1 in HSCs, where it is localized within the ER

Currently, the mechanisms by which HSCs respond to ER stress remain largely unknown. In this study, we sorted HSCs from DMSO- and tunicamycin-treated mice and performed RNA sequencing (RNA-seq).

Fig. 1 | Suppression of ER stress contributes to HSC maintenance during in vitro culture and IR-induced injury. A Experimental scheme. Lineage negative cells (Lin^- cells) or HSCs ($CD48^-CD150^+LSK$) were cultured in a liquid medium with DMSO, tunicamycin (5 μM), or azoramide (15 μM) for 24 h, followed by subsequent experiments. **B** Representative flow plots of the LSK ($Lin^-Sca\text{-}1^+c\text{-}Kit^+$) and HSCs ($CD48^-CD150^+LSK$) populations. Right graph represents the cell frequency of LSK and HSCs in cultured cells ($n = 3$ samples per group). **C** Representative images of the first (1st) and second (2nd) plating colonies. The scale bar represents 100 μm. Right graph represents the colony numbers ($n = 3$ samples per group). **D** Representative flow plots of the chimerism of peripheral blood (PB) from recipients at 1 and 4 months after transplantation. **E** The percentages of donor-derived cells in PB ($n = 5$ recipients per group). **F** The percentages of donor-derived BM cells, LK ($Lin^-Sca\text{-}1^-c\text{-}Kit^+$), LSK, and HSCs in BM of recipients at 4 months after transplantation ($n = 5$ recipients per group). **G** Experimental scheme. **H** Flow cytometry analysis of protein aggregate levels in HSCs ($CD48^-CD150^+LSK$) using ProteoStat staining. Right graph represents the mean fluorescence intensity (MFI) of ProteoStat in HSCs ($n = 4$ mice per group). FMO, Fluorescence-Minus-One Control. **I** Flow cytometry analysis of p-IRE1 and p-PERK staining in HSCs. Right graph represents the MFI of p-IRE1 and p-PERK in HSCs ($n = 4$ mice per group). **J** Experimental scheme. HSCs were treated with DMSO or azoramide (15 μM) for 24 h, followed by a dose of 2 Gy γ-irradiation and subsequent competitive transplantation. **K** The percentages of donor-derived cells in PB at indicated times ($n = 5$ recipients per group). **L** The percentages of donor-derived myeloid cells ($CD11b^+$), B cells ($B220^+$), and T cells ($CD3^+$) in PB cells of recipient mice at 4 months after transplantation ($n = 5$ recipients per group). **M** The percentages of donor-derived BM cells, LK, LSK, and HSCs in BM of recipients at 4 months after transplantation ($n = 5$ recipients per group). All statistical analyses were performed using two-tailed unpaired Student's *t*-test. Data are shown as mean ± SD. Results are representative of two independent experiments. Source data are provided as a Source Data file.

We observed that tunicamycin-induced ER stress significantly altered gene expression in HSCs, resulting in both upregulated and downregulated genes (>twofold change, $p < 0.05$) (Fig. 2A). Gene set enrichment analysis (GSEA) revealed that ER stress activates specific pathways such as apoptosis, p53, and TNF signaling via NF-κB pathway (Fig. 2B). To further investigate the response of HSCs to ER stress, an assay for transpose-accessible chromatin sequencing (ATAC-seq) was performed. We found that tunicamycin-treated HSCs displayed global chromatin opening, as evidenced by a significant increase in global ATAC-seq compared to DMSO-treated HSCs (Fig. 2C, D). The major signaling pathways enriched with the genes whose loci were associated with significantly changed ATAC-seq peaks upon ER stress are shown in Fig. 2E. Additionally, we conducted an overlap analysis of the RNA-seq and ATAC-seq databases focusing on genes showing upregulated ATAC peak and expression. *Bcl2a1a* was one of the mostly upregulated genes (Fig. 2F), which has been demonstrated the anti-apoptotic function in hematopoietic stem and progenitor cells[30]. Among other notable genes, we identified an intriguing gene, *Emp1* (Fig. 2F), which is a member of the PMP22 gene family[16]. Previous studies have reported that EMP1 plays critical roles in various stem cell types, including colorectal cancer stem-like cells and LSCs[17,18]. The increased expression of *Emp1* in HSCs under ER stress suggests its significant involvement in the ER response. To clarify the expression of *EMP1* in human hematopoietic cells, we analyzed published single-cell RNA sequencing (scRNA-seq) data[31] from human BM cells of five healthy donors. Our findings indicate that *EMP1* is most highly expressed in HSCs (Fig. S3A, B). Next, we characterized the expression of *Emp1* in subsets of primitive and mature BM cells from mice through quantitative reverse transcription polymerase chain reaction (qRT-PCR). Our findings revealed that *Emp1* exhibited the highest expression in HSCs ($CD48^-CD150^+LSK$) compared to LSK, LK, multipotent progenitor cells (MPPs), and mature cells (Fig. 2G). Collectively, these data demonstrate that *EMP1* is highly expressed in HSCs and may function as a potential responder to ER stress within this cell population.

To ascertain whether EMP1 is an ER protein, we isolated the ER from BM $Lin^-c\text{-}Kit^+$ cells derived from *wild-type* C57BL/6J mice, along with residual components. Western blot analysis demonstrated that EMP1 was predominantly present in ER extracts, as indicated by established ER markers such as protein disulfide isomerase and Calreticulin; conversely, it was absent in extracts devoid of ER (Fig. S3C). Similar results were observed in $CD34^+$ cells derived from human cord blood (Fig. S3C). Furthermore, immunofluorescence staining revealed that EMP1 co-localized with established ER marker Calreticulin in HSCs ($CD48^-CD150^+LSK$) (Fig. 2H). These findings confirm that EMP1 primarily resides within the ER in HSCs. Further characterization revealed that under ER stress, there was a significant increase in EMP1 protein levels in HSCs as determined by intracellular protein staining for flow cytometry (Fig. 2I). Given that IR induces ER stress in HSCs, we investigated the effect of IR on EMP1 expression and observed a significant elevation at both mRNA and protein levels in IR-treated HSCs compared to control (Fig. 2J, K). Collectively, these findings indicate that EMP1 is localized to the ER in HSCs, and that ER stress triggers the expression of EMP1.

Emp1 deficiency impairs HSC maintenance and self-renewal

To investigate the role of EMP1 in HSCs, we generated a conditional knock-out allele of *Emp1* ($Emp1^{fl/+}$), in which exons 3 to 4 are flanked with *loxP* sites. We then bred $Emp1^{fl/+}$ mice with *Tie2-Cre* mice, in which *Cre* recombinase is expressed in endothelial and hematopoietic cells under the control of *Tie2* promoter, to generate control $Emp1^{fl/fl}$ mice and $Emp1^{fl/fl}$, *Tie2-Cre*, with conditional deletion of *Emp1* (named as *Emp1-cKO* mice) (Fig. S4A). The efficiency of *Emp1* deletion in BM cells and HSCs was validated through western blot analysis and qRT-PCR, respectively (Fig. S4B). At 2 months of age, *Emp1-cKO* mice showed no obvious changes in hematological parameters compared to $Emp1^{fl/fl}$ mice (Fig. S4C). The frequency of myeloid, red, B, and T cells was similar between $Emp1^{fl/fl}$ and *Emp1-cKO* mice (Fig. S4D–O). However, BM cellularity was decreased in *Emp1-cKO* mice compared to controls (Fig. 3A). Subsequent cell surface marker staining revealed that there were significantly fewer hematopoietic stem and progenitor cells in BM of *Emp1-cKO* mice than that of $Emp1^{fl/fl}$ mice. This included LK cells (common myeloid progenitors [CMPs], granulocyte-erythroid progenitors, and megakaryocyte-erythroid progenitors [MEPs]), LSK cells, and short-time HSCs (ST-HSCs), multipotent progenitors (MPPs), lymphoid-primed multipotent progenitors (LMPPs), and HSCs (defined as $CD48^-CD150^+LSK$ or $CD34^-CD135^-LSK$) (Fig. 3B–F). To further determine the abundance of functional HSCs, we performed a limiting dilution assay and observed a significant reduction in the frequency of functional HSCs in *Emp1-cKO* mice compared to that in $Emp1^{fl/fl}$ mice (1/40916 in *Emp1-cKO* versus 1/5852 in $Emp1^{fl/fl}$) (Fig. 3G).

The CFU assay demonstrated that *Emp1*-deficient HSCs produced a significantly reduced number of total colonies compared to $Emp1^{fl/fl}$ HSCs in the first and second plating (Fig. S5A, B), indicating that *Emp1* deficiency impaired the proliferation of *Emp1-cKO* HSCs in vitro. Additionally, we administered the cell cycle-dependent myelotoxic agent 5-fluorouracil (5-FU) into mice on a weekly basis. The poor survival of *Emp1-cKO* mice indicated defective hematopoiesis in comparison to control mice (Fig. S5C). To further assess the hematopoietic potential of HSCs in vivo, we transplanted HSCs into lethally irradiated recipient mice (CD45.1) and evaluated the hematopoiesis of recipients at two months post-transplantation (Fig. S5D). Our findings revealed that *Emp1* deficiency compromised the repopulation potential of HSCs, as evidenced by significantly reduced PB cells and BM cellularity in recipient mice (Fig. S5E, F). Furthermore, the recipient mice derived from *Emp1-cKO* HSCs exhibited a considerably decreased number of LK, LSK, MPP, LMPP, ST-HSCs, and HSCs in BM compared to control recipients (Fig. S5G–J). Taken together, these data suggest that *Emp1* is crucial for maintaining HSC function and supporting hematopoiesis.

https://doi.org/10.1038/s41467-025-61552-0

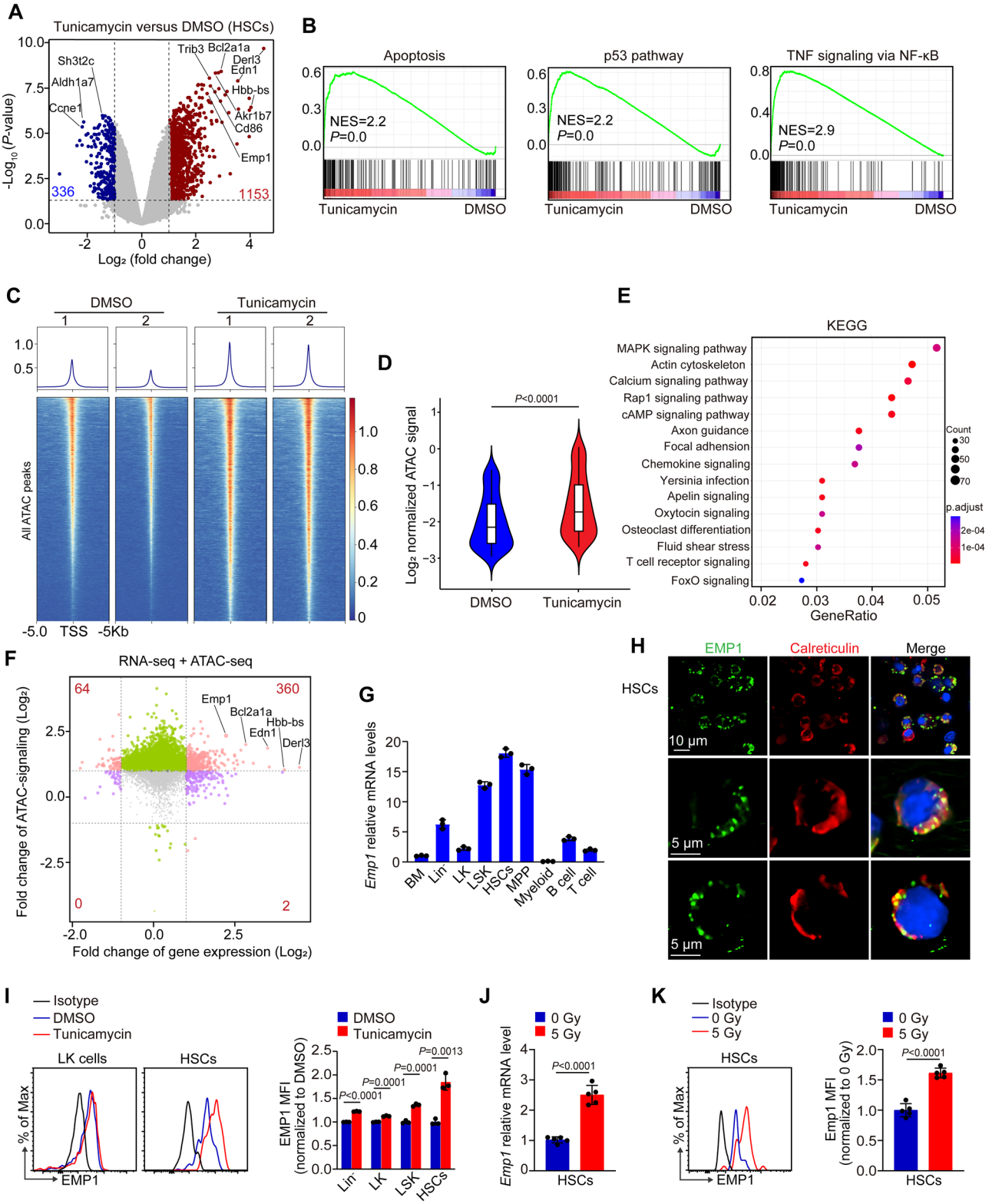

To further evaluate the long-term self-renewal capacity of HSCs, we performed a competitive serial transplantation assay. The sorted *Emp1*$^{fl/fl}$ or *Emp1-cKO* HSCs (CD45.2) were mixed with competitive BM cells (CD45.1CD45.2) and then transplanted into lethally irradiated recipient mice (CD45.1) (Fig. S6A). Donor-derived PB cells from *Emp1-cKO* HSCs showed continuously decreased chimeric percentages compared to control (Fig. S6B, C). Additionally, the chimeric percentages of mature cells in PB showed a consistent decrease as well (Fig. S4D). The reduced percentages of BM cells, LK, LSK, and HSCs in recipient mice indicate that *Emp1* deficiency impairs the self-renewal of HSCs (Fig. S6E). To investigate whether *Emp1* regulates the self-renewal of HSCs in a cell-intrinsic manner, BM cells (CD45.2) from *Emp1*$^{fl/fl}$ and *Emp1*$^{fl/fl}$*, Mx1-Cre* mice were mixed with competitor BM cells (CD45.1CD45.2) and transplanted into lethally irradiated recipient mice (CD45.1). Subsequently, the recipient mice received injections of polyinosinic:polycytidylic acid (pIpC) at 1 month after transplantation

Fig. 2 | ER stress induces the expression of EMP1 in HSCs, where it is localized within the ER. A A representative volcano plot of the gene expression changes between HSCs from DMSO-treated and tunicamycin-treated mice ($n = 5$ mice per group). All significantly changed genes (>twofold change, $P < 0.05$) are indicated by blue or red dots. **B** GSEA shows that apoptosis, p53, and TNF signaling via NF-κB pathways are significantly upregulated in tunicamycin-treated HSCs compared to DMSO-treated HSCs. **C** Representative heatmaps show ATAC-seq peaks ± 5 kb from transcriptional start site (TSS) in HSCs. Top, line plots of relative quantifications based on average intensities of all ATAC peaks detected. **D** Statistics and quantification of genomic-wide ATAC signal ($n = 2$ samples per group). Violin plot of the $\log_2$(normalized RPKM) of peaks under different conditions. The box plot represents the minimum, median, and maximum values. **E** The KEGG analysis of the enrichment and classification of the significantly changed peaks. **F** The quadrant chart shows the distribution of genes with both differential ATAC peaks and differential expression in the tunicamycin-treated HSCs compared with the control group. **G** qRT-PCR analysis of *Emp1* expression in different hematopoietic cell subsets in *wild-type* mice ($n = 3$ mice per group), including BM cells, Lin^- cells, LK, LSK, MPP ($CD48^+CD150^-LSK$), myeloid cells ($Gr1^+CD11b^+$), B cells ($B220^+$), and T cells ($CD3^+$). **H** Immunofluorescence staining of EMP1 (green) and Calreticulin (red) in murine HSCs ($CD48^-CD150^+LSK$). Nuclei are stained with DAPI (blue). **I** Flow cytometry analysis of EMP1 staining in LK cells and HSCs ($CD48^-CD150^+LSK$) from DMSO-treated and tunicamycin-treated mice. Right graph represents the MFI of EMP1 in hematopoietic cells ($n = 3$ mice per group). **J** qRT-PCR analysis of *Emp1* expression in HSCs ($CD48^-CD150^+LSK$). HSCs are isolated from *wild-type* mice that were exposed to 0 or 5 Gy radiation ($n = 5$ mice per group). **K** Flow cytometry analysis of EMP1 staining in HSCs. Right graph represents the MFI of EMP1 in HSCs ($n = 5$ mice per group). All statistical analyses were performed using two-tailed unpaired Student's *t*-test. Data are shown as mean ± SD. Results are representative of two independent experiments. Source data are provided as a Source Data file.

to induce *Emp1* deletion, followed by chimerism analysis and second transplantation (Fig. 3H). The decreased chimeric percentages of PB, BM cells, LK, LSK, and HSCs suggested that *Emp1* loss impaired the self-renewal of HSCs in a cell-intrinsic manner (Fig. 3I–L). Additionally, we enforced *Emp1* expression in HSCs via retrovirus and transplanted transduced HSCs (CD45.1) into lethally irradiated recipient mice (CD45.2) with competitor BM cells (CD45.1CD45.2) (Fig. S6F). We observed that the donor-derived cells from *Emp1*-overexpressed HSCs exhibited continuously increased chimeric percentages of PB and BM cells in recipient mice compared to control group (Fig. S6G–I), indicating that *Emp1* overexpression promoted self-renewal of HSCs. Collectively, these data demonstrate that *Emp1* is essential for long-term self-renewal of HSCs.

Emp1 deficiency leads to the formation of protein aggregates and ER stress in HSCs

Quiescence is a fundamental characteristic of HSCs that ensures longevity[8]. In this study, we conducted Ki-67 + DAPI staining and observed a lower proportion of quiescent $CD48^-CD150^+LSK$ (G0 phase) in *Emp1-cKO* mice (47.4%) compared to control mice (62.0%) (Fig. 4A). Additionally, staining with annexin-V and DAPI revealed an increased rate of early/late apoptosis in $CD48^-CD150^+LSK$ lacking *Emp1* function (Fig. 4B). To investigate the molecular mechanisms underlying *Emp1*-regulated HSC homeostasis, we performed RNA-seq analysis on freshly sorted HSCs from both $Emp1^{fl/fl}$ and *Emp1-cKO* mice. Our analysis identified 163 significantly upregulated genes and 316 considerably downregulated genes (>twofold change; $p < 0.05$) in *Emp1-cKO* HSCs compared to controls (Fig. 4C). Furthermore, gene ontology (GO) analysis of the RNA-seq data highlighted significant dysregulation in genes associated with myeloid cell differentiation and regulation of hematopoiesis in HSCs lacking EMP1 function (Fig. 4D). E2F1 is known as a positive regulator for cell cycle progression[32]. GSEA of the RNA-seq data demonstrated a significant up-enrichment of E2F1 target-associated genes in *Emp1-cKO* HSCs compared to control. Moreover, GSEA also revealed an up-enrichment of genes associated with ER stress response, also known as UPR, in *Emp1-cKO* HSCs (Fig. 4E).

Based on previous findings, including the localization of EMP1 to ER (Fig. 2H), upregulation of *Emp1* in HSCs in response to ER stress (Fig. 2I), and the observation that *Emp1* deficiency leads to an ER stress response at the transcriptional level in HSCs (Fig. 4E), it is suspected that EMP1 plays a role in governing ER stress in HSCs. Notably, *Emp1-cKO* HSCs exhibited a significantly increased level of protein aggregates compared to $Emp1^{fl/fl}$ HSCs (Fig. 4F). Furthermore, key markers of ER stress response, such as Glucose regulatory protein 78, p-PERK, p-eIF2α, ATF4, and p-IRE1 were found to be significantly elevated in *Emp1-cKO* HSCs compared to $Emp1^{fl/fl}$ HSCs (Fig. 4G). Additionally, there was an observed increase in expression of CCAAT-enhancer-binding protein homologous protein (CHOP) in *Emp1*-cKO HSCs (Fig. 4H), a molecule involved in ER stress-induced apoptosis[33]. Elevated ER stress often causes ER morphology change[34]. Compared to normal ER morphology of $Emp1^{fl/fl}$ HSCs, ER of *Emp1-cKO* HSCs showed intensified edema and expansion, as noted by white arrows (Fig. 4I). Heat stress serves as an additional induction condition for the formation of protein aggregates and subsequent ER stress[35]. We cultured HSCs at temperatures of 37 °C or 42 °C for a duration of one hour (Fig. S7A). Our observation revealed that *Emp1-cKO* HSCs exhibited a higher level of protein aggregates compared to $Emp1^{fl/fl}$ HSCs (Fig. S7B), along with elevated levels of key markers associated with the ER stress response, specifically p-IRE1 and p-PERK (Fig. S7C).

To further investigate the function of *EMP1* in regulating human hematopoietic stem and progenitor cells (HSPCs), we utilized short hairpin RNA (shRNA) lentivirus to knock down *EMP1* expression specifically within $CD34^+$ hematopoietic cells derived from human cord blood. The results showed a significant increase in protein aggregates when *EMP1* expression was reduced (Fig. 4J), along with an elevated rate of apoptosis among shEMP1-transduced $CD34^+$ cells as opposed to shControl cells (Fig. 4K). Additionally, we observed a decrease in the frequency of quiescent $CD34^+$ cells (cells in G0 phase) when EMP1 expression was diminished through shRNA intervention (Fig. S7D). In summary, these data demonstrate that knock-out or knock-down of *EMP1* results in protein aggregation and subsequent induction of ER stress in murine HSCs and human HSPCs, respectively.

Loss of Emp1 aggravates HSC defects under IR conditions

Given that radiation induces ER stress in HSCs, we hypothesize that EMP1 might play a crucial role in regulating the susceptibility of HSCs to IR. To investigate this hypothesis, $Emp1^{fl/fl}$ and *Emp1-cKO* mice were exposed to various doses (2, 5, or 7.5 Gy) of γ-irradiation (Fig. 5A). The loss of *Emp1* significantly reduced the survival time of mice compared to control mice under IR-induced injury (Fig. 5B), indicating increased susceptibility of *Emp1-cKO* mice to IR. Furthermore, we observed intensified loss of hematopoietic cells in *Emp1-cKO* mice compared with $Emp1^{fl/fl}$ mice under IR conditions (2 Gy), as evidenced by significantly reduced numbers of BM cells, LK, LSK, and HSCs (Fig. 5C–G). Additionally, we found that the loss of *Emp1* aggravated HSC defects under IR conditions, as indicated by higher levels of protein aggregates (Fig. 5H), markers of ER stress response such as phosphorylated IRE1 and PERK proteins (p-IRE1 and p-PERK) (Fig. 5I, J), and increased apoptosis rates (Fig. 5K). In addition to inducing apoptosis, IR also facilitates the exit of HSCs from quiescence, thereby further accelerating HSC exhaustion[24]. Staining with Ki-67 and DAPI revealed that the proportion of quiescent HSCs in IR-treated $Emp1^{fl/fl}$ mice was lower than that observed in non-IR-treated $Emp1^{fl/fl}$ mice (34.6% versus 59.2%) (Fig. 5L). Moreover, the deficiency of *Emp1* exacerbated this phenomenon, resulting in the lowest proportion of quiescent HSCs in IR-treated *Emp1-cKO* mice (18.9%) (Fig. 5L). Collectively, these findings demonstrate that the loss of *Emp1* aggravates HSC defects under IR conditions.

https://doi.org/10.1038/s41467-025-61552-0

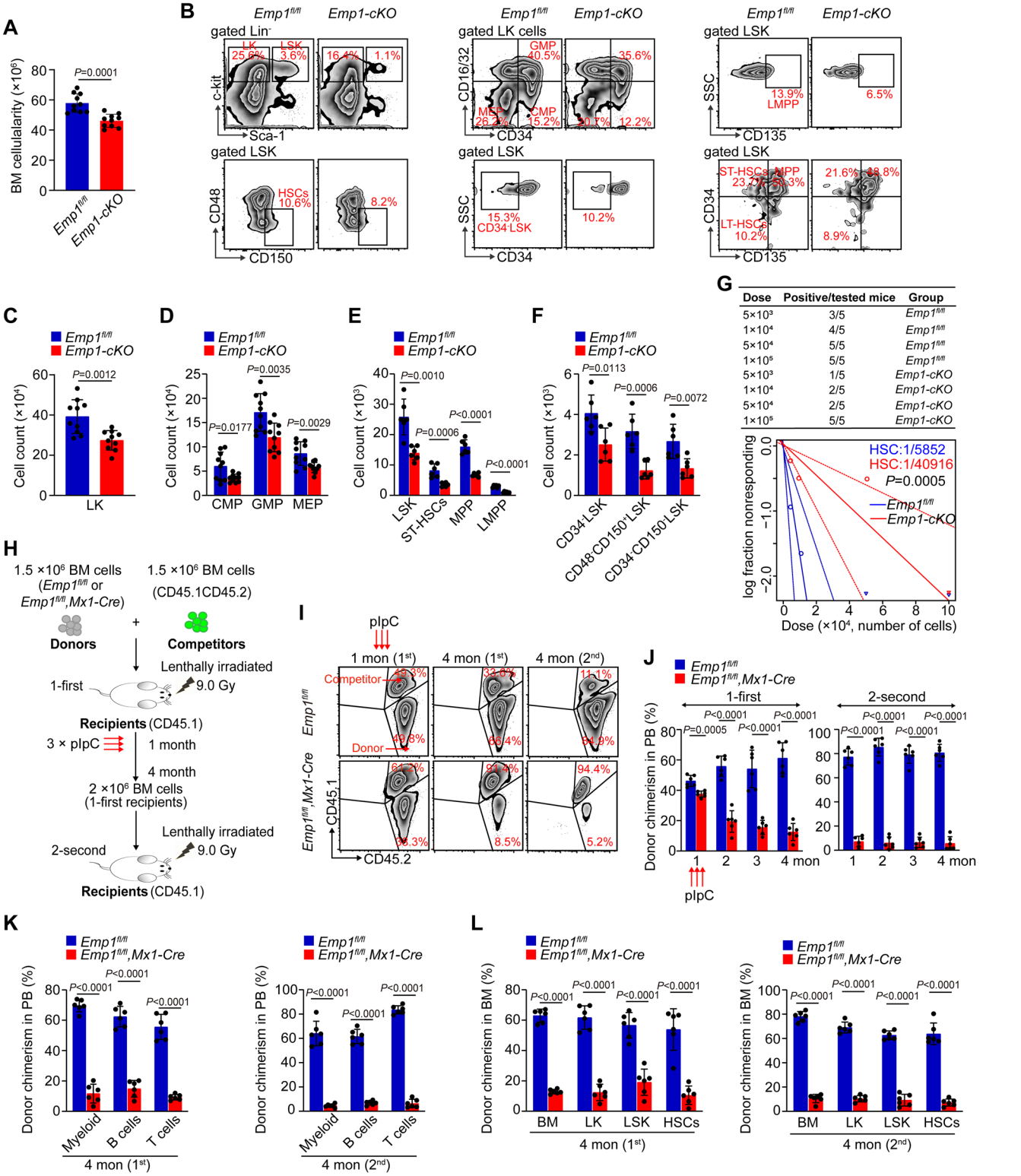

Loss of Emp1 results in the accumulation of dhCer in HSCs

To further investigate the underlying cause of protein aggregate accumulation in HSCs due to *Emp1* deficiency, we performed an untargeted metabolomics analysis utilizing ultra-high-performance liquid chromatography-mass spectrometry (UHPLC-MS/MS) on sorted *Emp1*$^{fl/fl}$ and *Emp1-cKO* HSCs. A total of 283 metabolites with MS/MS matching score >0.3 have been identified, revealing 33 differential metabolites between *Emp1*$^{fl/fl}$ and *Emp1-cKO* HSCs (Variable Importance in the Project [VIP] > 1.0; $p < 0.05$) (Fig. 6A) (Supplementary Data 1). KEGG analysis of the metabolomics data indicated that the sphingolipid signaling pathway was significantly dysregulated between *Emp1*$^{fl/fl}$ and *Emp1-cKO* HSCs (Fig. 6B). Sphingolipids are ubiquitous and essential components of all eukaryotic membranes[36]. Ceramide is the central component of all complex sphingolipids, including sphingomyelin and glycosphingolipids (Fig. 6C)[37]. Bioactive sphingolipid metabolites have been recognized as important molecular players in metabolic diseases, and perturbed sphingolipid metabolism contributes to HSC dysfunction[38]. Subsequent lipidomic analysis using

Fig. 3 | *Emp1* deficiency impairs HSC maintenance and self-renewal. **A** Quantification of BM cellularity of *Emp1*$^{fl/fl}$ and *Emp1*$^{fl/fl}$, *Tie2-Cre* (named *Emp1-cKO*) mice at 2 months of age ($n = 10$ mice per group). **B** Representative flow plots of LK (Lin$^-$Sca-1$^-$c-Kit$^+$), LSK (Lin$^-$Sca-1$^+$c-Kit$^+$), CMP (CD34$^+$CD16/32^{med}LK), MEP (CD34$^-$CD16/32$^-$LK), GMP (CD34$^+$CD16/32$^+$LK), MPP (CD34$^+$CD135$^+$LSK), LMPP (CD135^{high}LSK), ST-HSC (CD34$^+$CD135$^-$LSK), CD34$^-$LSK, HSC (CD48$^-$CD150$^+$LSK or CD34$^-$CD135$^-$LSK) population in BM of *Emp1*$^{fl/fl}$ and *Emp1-cKO* mice. **C**–**F** Graphs represent the cell count of different hematopoietic cell subsets in BM of mice (**C** and **D**, $n = 10$ mice per group; **E** and **F**, $n = 6$ mice per group). **G** The HSC frequency was calculated and the log-fraction plot was generated using extreme limiting dilution analysis ($n = 5$ recipient mice at each cell concentration). A positive response was considered if donor engraftment in the BM of recipient mice exceeded 1% for both lymphoid and myeloid lineages at 12 weeks post-transplantation. **H** Experimental schematic for the competitive transplantation assay. **I** Representative flow plots of the chimerism of PB from recipients in serial competitive transplantation assay. Donor-derived cells, CD45.2$^+$; competitor-derived cells, CD45.1$^+$CD45.2$^+$. **J** The percentages of donor-derived cells in PB at indicated times ($n = 6$ recipients per group). **K** The percentages of donor-derived myeloid cells, B cells, and T cells in PB cells of recipient mice at 4 months after first and second transplantation ($n = 6$ recipients per group). **L** The percentages of donor-derived BM cells, LK, LSK, and HSCs in BM of recipients at 4 months after first and second transplantation ($n = 6$ recipients per group). All statistical analyses were performed using two-tailed unpaired Student's *t*-test. Data are shown as mean ± SD. Results are representative of two independent experiments. Source data are provided as a Source Data file.

UHPLC-MS/MS revealed a significant increase in dihydroceramides (dhCer), particularly dhCer (d18:0/24:1), in HSCs as a result of *Emp1* deficiency (Fig. 6D) (Supplementary Data 2).

The recent findings demonstrate that the ratio of protein to sphingolipids directly determines the rate of protein aggregates[39]. To explore the effect of dhCers on HSC function, we cultured murine HSCs (CD48$^-$CD150$^+$LSK) in vitro and introduced BODIPY TR C5-Ceramide into the medium for a duration of 30 min. Following this treatment, we observed pronounced red fluorescence in HSCs (Fig. S8A), indicating that these cells can take up ceramide. Subsequently, we directly added dhCer(d18:0/24:1) to the culture medium of HSCs and assessed their function in vitro and in vivo (Fig. 6E). Our observations revealed that the addition of dhCer(d18:0/24:1) significantly increased the level of protein aggregates in HSCs in vitro (Fig. 6F), leading to a remarkable decrease in colony-forming capacity of HSCs (Fig. 6G). Furthermore, pre-treatment with dhCer(d18:0/24:1) substantially impaired the reconstitution capacity of HSCs, as evidenced by continuously decreased chimeric percentages of PB and BM cells in recipient mice compared to control group (Fig. 6H–K). These data collectively indicate that the loss of *Emp1* leads to the accumulation of dhCer in HSCs. Furthermore, this accumulation of dhCer results in the formation of protein aggregates and adversely affects both in vitro and in vivo functions of HSCs.

EMP1 binds CERS2 to restrict dhCer production

The increased production or decreased consumption of dhCers could result in dhCer accumulation, a process catalyzed by several enzymes (Fig. 7A)[40]. As EMP1 is located within the ER, we aimed to screen for EMP1-interacting proteins to uncover the exact mechanisms by which EMP1 restricts dhCer accumulation. We overexpressed EMP1 (with HA tag) in BM Lin$^-$c-Kit$^+$ cells derived from *wild-type* mice. Subsequently, we performed co-immunoprecipitation (co-IP) followed by mass spectrometry using IgG or HA antibodies (Fig. 7B). Compared to the group using IgG antibody, 336 proteins were pulled down by the HA antibody, suggesting potential EMP1-interacting partners. Among these proteins, it was observed that EMP1 might interact with ceramide synthase 2 (CERS2) (Fig. 7C). The complete list of interacting proteins can be found in Supplementary Data 3. There are six enzymes in the CERS family, which are located in the ER membrane[41]. CERS2 prefers to use C22–C24-CoAs for the N-acylation of dihydrospingosine, resulting in the production of C22–C24 dhCers[40]. Considering the findings that *Emp1* deficiency resulted in a significant increase in the accumulation of dhCer(d18:0/22:0), dhCer(d18:0/22:1), and dhCer(d18:0/24:1) (Fig. 6D), along with the observation that neither tunicamycin-induced ER stress nor *Emp1* deficiency had a notable impact on the mRNA levels of CERS2 in HSCs (Fig. S8B), these results collectively suggest that EMP1 may limit dhCer accumulation by inhibiting CERS2 activity through protein interactions. To investigate this further, we overexpressed HA-EMP1 in BM Lin$^-$c-Kit$^+$ cells derived from *wild-type* mice. The interaction between EMP1 and CERS2 was confirmed through co-immunoprecipitation followed by immunoblot analysis (Fig. 7D). Additionally, an in situ proximity ligation assay (PLA) revealed that EMP1 physically interacted with CERS2 in HSCs (Fig. 7E).

To delve deeper into the molecular mechanism of interaction between EMP1 (AlphaFold prediction: AF-P47801-F1) and CERS2 (AlphaFold prediction: AF-Q924Z4-F1), we conducted a molecular docking assay and found an interaction between amino acid residues of EMP1 and the Tram-Lag-CLN8 (TLC) domain of CERS2, particularly within the Lag1p motif (Fig. 7G). It has been demonstrated that the Lag1p motif imparts acyl chain substrate specificity to the protein and is part of the catalytic domain of CERS2[41]. Furthermore, we forced expression of Flag-CERS2 or its mutant proteins—involving a total of 8 mutations on amino acid residues within the laglp motif—in BM Lin$^-$c-Kit$^+$ cells derived from *wild-type* mice, along with HA-EMP1 (Fig. 7G). The co-IP followed by immunoblot analysis confirmed the interaction between EMP1 and *wild-type* CERS2, but not with mutant CERS2 (Fig. 7H). To further investigate the universality of the protein interaction between EMP1 and CERS2 in other cell types, we performed a PLA assay using HEK293T cells; however, we did not observe obvious interaction signal between EMP1 and CERS2 in HEK293T cells (Fig. S8C). Furthermore, the knock-down of EMP1 did not result in a notable change in protein aggregation levels (Fig. S8D, E) or ER stress response in HEK293T cells (Fig. S8F), indicating that the EMP1-CERS2 axis is not universally applicable to various cell types.

To determine whether the dysregulation of CERS2 activity in *Emp1*-deficient HSCs contributes to the impaired maintenance of HSCs, we administrated pIpC injection to induce *Emp1* deletion and treated these mice with an inhibitor of CERSs, fumonisin B1 (FB1) (Fig. 7I). FB1 efficiently reduced the level of protein aggregates in *Emp1*-deficient HSCs (Fig. 7J). Importantly, FB1 treatment partially abolished the increased levels of p-IRE1 and p-PERK in *Emp1*-deficient HSCs, indicating alleviated ER stress (Fig. 7K). Furthermore, FB-1-treated *Emp1*-deficient mice showed significant restoration in the numbers of BM cells, LK, LSK, and HSCs (CD48$^-$CD150$^+$LSK) compared with their DMSO-treated counterparts (Fig. 7L–O). These findings collectively suggest that EMP1 interacts with the enzyme CERS2 to restrict dhCer accumulation, thereby constraining ER stress and preserving HSC maintenance.

Emp1 overexpression or CERS2 inhibition protects HSCs against IR-induced injury

To further evaluate whether overexpression of EMP1 protects HSCs against IR-induced injury, we enforced the expression of *Emp1* in *wild-type* HSCs (CD48$^-$CD150$^+$LSK) and subjected these transduced cells to a dose of 2 Gy IR followed by a competitive transplantation assay (Fig. 8A). Flow cytometry analysis demonstrated that irradiated HSCs exhibited less than 10% chimerism in PB and BM of recipient mice. However, in contrast, overexpression of *Emp1* substantially enhanced the engraftment capacity of IR-treated HSCs, as evidenced by the gradually increased donor-derived cells in PB and BM (Fig. 8B–D).

Given that EMP1 primarily interacts with CERS2, we hypothesized that the inhibition of CERS2 could protect HSCs from IR exposure. To explore this hypothesis, HSCs (CD48$^-$CD150$^+$LSK) derived from *wild-type* mice were treated with FB1 (10 μM) for 24 h to inhibit CERS2

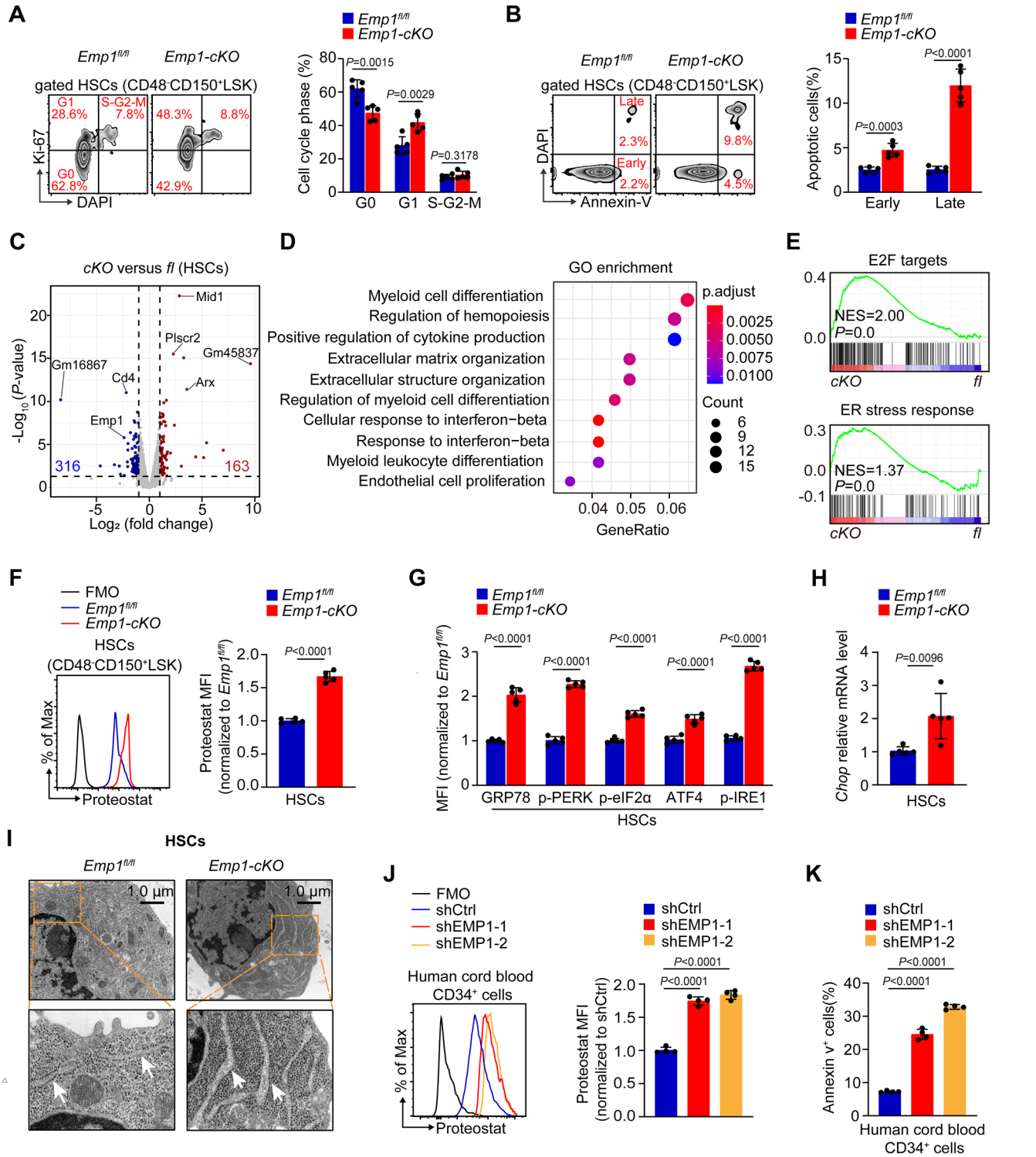

activity. Subsequently, the HSCs were exposed to a dose of IR (2 Gy), and after 24 h, they were analyzed by flow cytometry for phenotypic characterization or transplanted into recipient mice (Fig. 8E). Our findings indicated that the inhibition of CERS2 partially mitigated HSC defects under IR conditions, as evidenced by reduced levels of protein aggregates (Fig. 8F) and markers related to ER stress response, including phosphorylated IRE1 and PERK proteins (Fig. 8G). For the competitive transplantation assay, it was observed that IR treatment significantly reduced the chimeric percentages of donor-derived PB, BM cells, LSK, and HSCs in recipient mice compared to the non-IR-treated group. The administration of FB1 did not significantly impact the reconstitution capacity of HSCs that were not subjected to IR treatment. Encouragingly, it markedly enhanced the reconstitution capacity of IR-treated HSCs in recipient mice (Fig. 8H–J). These findings collectively demonstrate that *Emp1* overexpression or CERS2 inhibition effectively protects HSCs against IR-induced injury. These findings highlight the critical role played by the EMP1-CERS2-dhCers axis in constraining ER stress and preserving HSC potential (Fig. 8K).

Discussion

EMP1 has been identified as a prognostic factor in MDS[18] and AML[19], as well as a stemness-related gene in LSCs[20], suggesting the crucial

Fig. 4 | *Emp1* deficiency leads to the formation of protein aggregates and induces ER stress in HSCs. A Representative flow plots of the Ki-67 and DAPI staining of HSCs ($CD48^-CD150^+LSK$). Right graph represents the percentages of cell-cycle distribution of HSCs ($n = 5$ mice per group). **B** Representative flow plots of the Annexin-V and DAPI staining of HSCs ($CD48^-CD150^+LSK$). Right graph represents the percentages of apoptotic HSCs ($n = 5$ mice per group). Early apoptotic cells, Annexin-V^+DAPI^-; Late apoptotic cells, Annexin-V^+DAPI^+. **C** A representative volcano plot of the gene expression changes between $Emp1^{fl/fl}$ and *Emp1-cKO* HSCs ($CD48^-CD150^+LSK$) ($n = 3$ samples per group). All significantly changed genes (>twofold change, $P < 0.05$) are indicated by blue or red dots. **D** The Gene Ontology (GO) analysis of the enrichment and classification of the differentially expressed genes. **E** GSEA shows that E2F targets and ER stress response pathways are significantly upregulated in *Emp1-cKO* HSCs compared to $Emp1^{fl/fl}$ HSCs. **F** Flow cytometry analysis of protein aggregate levels in HSCs using ProteoStat staining. Right graph represents the MFI of ProteoStat in HSCs ($CD48^-CD150^+LSK$) ($n = 5$ mice per group). **G** A graph represents the MFI of indicated proteins in HSCs ($CD48^-CD150^+LSK$) using flow cytometry staining and analysis ($n = 5$ mice per group). **H** qRT-PCR analysis of *Chop* expression in $Emp1^{fl/fl}$ and *Emp1-cKO* HSCs ($CD48^-CD150^+LSK$) ($n = 5$ mice per group). **I** Representative electron microscopic images of $Emp1^{fl/fl}$ and *Emp1-cKO* HSCs ($CD48^-CD150^+LSK$). The white arrows indicate the presence of changed ER morphology. **J** Flow cytometry analysis of protein aggregate levels in human cord blood $CD34^+$ cells using ProteoStat staining. $CD34^+$ cells were infected with shRNA lentivirus targeting EMP1 and control shRNA lentivirus. Right graph represents the MFI of ProteoStat ($n = 4$ samples per group). **K** A graph represents the percentages of apoptotic human cord blood $CD34^+$ cells ($n = 4$ samples per group). All statistical analyses were performed using two-tailed unpaired Student's *t*-test. Data are shown as mean ± SD. Results shown in (**A**, **B** and **F**–**K**) are representative of two independent experiments. Source data are provided as a Source Data file.

functions of EMP1 in leukemogenesis. In addition to its role in leukemia, EMP1 is highly expressed in several cancers and regulates their proliferation, migration, and stemness[16]. $EMP1^+$ cells are responsible for the metastatic recurrence in colorectal cancer[17]. It has been reported that EMP1 regulates the PI3K-AKT signaling in gliomas cells[42] and the gastric cancer cells[43], and activates MAPK pathway in ovarian cancer cells[44]. However, the exact molecular function of EMP1 in cells has long been unknown. Here, we have identified a previously unrecognized role for EMP1 in the maintenance and self-renewal of HSCs. Deletion of *Emp1* leads to quiescence exit and apoptosis of HSCs, exhaustion of the HSC pool and eventually defective hematopoiesis. Mechanistically, EMP1 localizes to the ER in HSCs and directly binds CERS2 to restrict dhCer production. HSCs are susceptible to dhCer accumulation, which impairs HSC function by inducing protein aggregation and ER stress. Therefore, EMP1 safeguards HSC function by constraining ER stress. This study uncovers the precise localization and molecular function of EMP1. Further investigation is needed to determine whether the EMP1-CERS2-sphingolipid metabolism-ER stress pathway exists in other cell types, particularly in leukemia cells.

To ensure the long-term health of HSCs, it is crucial to maintain protein homeostasis[45]. HSCs rely on unique strategies to precisely regulate the process of protein synthesis, folding, and quality control[46]. In comparison to other hematopoietic cells, HSCs exhibit the lowest rate of protein synthesis, even under conditions of cell division[47]. To achieve diverse functions, proteins fold into specific enabling structures or ensembles. However, this process inevitably causes protein misfolding, leading to the generation of protein aggregates and resulting in ER stress. The SEL1L-HRD1 complex, which is the most conserved branch of ER-associated degradation, is highly expressed in HSCs, indicating its efficiency in degrading misfolded proteins[13]. Additionally, it has been reported that HSCs preferentially traffic misfolded proteins to aggresomes and depend on aggrephagy to maintain protein homeostasis[46]. This study defines that the production of dhCers in the ER is restricted to prevent the accumulation of protein aggregates in HSCs. Thus, we uncover an unrecognized proteostasis mechanism to safeguard the HSC pool through sphingolipid metabolism, along with mechanisms for constraining protein synthesis and degrading misfolded proteins. Although the maintenance of HSCs requires a low-dose ER stress response, both intrinsic and extrinsic signaling often lead to elevated ER stress, ultimately impairing HSC function[11]. The loss of CHOP, a factor that induces cell death in response to ER stress, significantly improves the repopulation capacity of HSCs[48]. Additionally, deletion of transmembrane protein 166, a downstream factor of CHOP, efficiently enhances the regeneration capacity of HSCs by inhibiting ER stress-induced apoptosis[49]. HSCs rely on several critical factors to constrain ER stress. For example, hypoxia-inducible factor 2α (HIF-2α) protects HSCs by reducing ROS and ER stress[50], while the RNA binding protein Dppa5 is highly expressed in HSCs and improves their function by reducing ER stress[51]. In this study, we found that loss of *Emp1* resulted in the accumulation of dhCer and increased ER stress in HSCs. This suggests a protective role for EMP1 in HSCs by constraining ER stress. Together, these findings suggest a complex network within HSCs that constrains ER stress involving factors such as HIF-2α, Dppa5, and EMP1. The interplay or coordination between these factors needs to be further clarified.

Sphingolipids are a diverse group of structurally complex lipids, and maintaining sphingolipid homeostasis is crucial for the proper function of HSCs[36]. The loss of serine palmitoyltransferase (SPT) long-chain base subunit 1 (SPTLC1), which catalyzes the initial and rate-limiting step in sphingolipid biosynthesis, leads to the accumulation of fatty acids and subsequent ER stress in HSPCs[38]. Sphingolipid delta4-desaturase (DEGS1) is an ER-membrane-spanning protein that serves as the final enzyme in de novo sphingolipid synthesis, converting dhCers to Cers[41]. Knock-down of DEGS1 in human cord blood stem cells results in an increased ratio of dhCers/Cers and ultimately impairs the reconstitution capacity of HSPCs[52], indicating that timely conversion of dhCers to Cers is essential for HSPC homeostasis. Given the higher expression of DEGS1 and lower levels of dhCers in HSCs compared to hematopoietic progenitor cells and mature cells[52], it appears that HSCs particularly require low levels of dhCers. Recent research has identified sphingolipids as critically important bioactive substances. Very long chain ceramides (VLC Cers) are significant contributors to inflammation and directly regulate the nuclear translocation of key immune-related transcription factor REL. A hypothesis has been proposed suggesting that "the pool size of VLC Cers may directly regulate REL activity."[53]. A more direct finding indicates that, compared to conditions without the addition of Cers, the presence of a 1:1 ratio of protein to Cers significantly increases the level of protein aggregation[39]. These findings suggest that sphingolipids directly alter the properties and functions of proteins. In this study, we demonstrate that dhCers are bioactive molecules. Their accumulation leads to protein aggregation and ER stress in HSCs. DhCers within the ER may directly interact with proteins in the ER lumen, hindering their proper folding and leading to the formation of protein aggregates, which ultimately results in excessive ER stress. These findings expand our understanding of how sphingolipid metabolism regulates HSC homeostasis and reveal an unrecognized source of ER stress—namely, accumulation of dhCers.

CERS2 is the most abundantly expressed member of the CERS gene family, responsible for mediating N-acylation of dihydrospingosine to form dhCers[54]. The activity of CERS2 supports various biological functions, including the maintenance of myelin, stabilization of the cerebellar, protection against hepatocarcinomas[54], maintenance of colonic macrophage populations[53], and muscle homeostasis[55]. The precise regulation of CERS2 activity largely depends on partner interaction. Acyl-coenzyme A-binding protein (ACBP) binds long-chain and very-long-chain acyl-CoA esters to increase the activity of CERS2[56]. BCL2-like 13 (BCL2L13) protein has been shown to bind CERS2 and inhibit its activity in glioblastoma[57]. In

https://doi.org/10.1038/s41467-025-61552-0

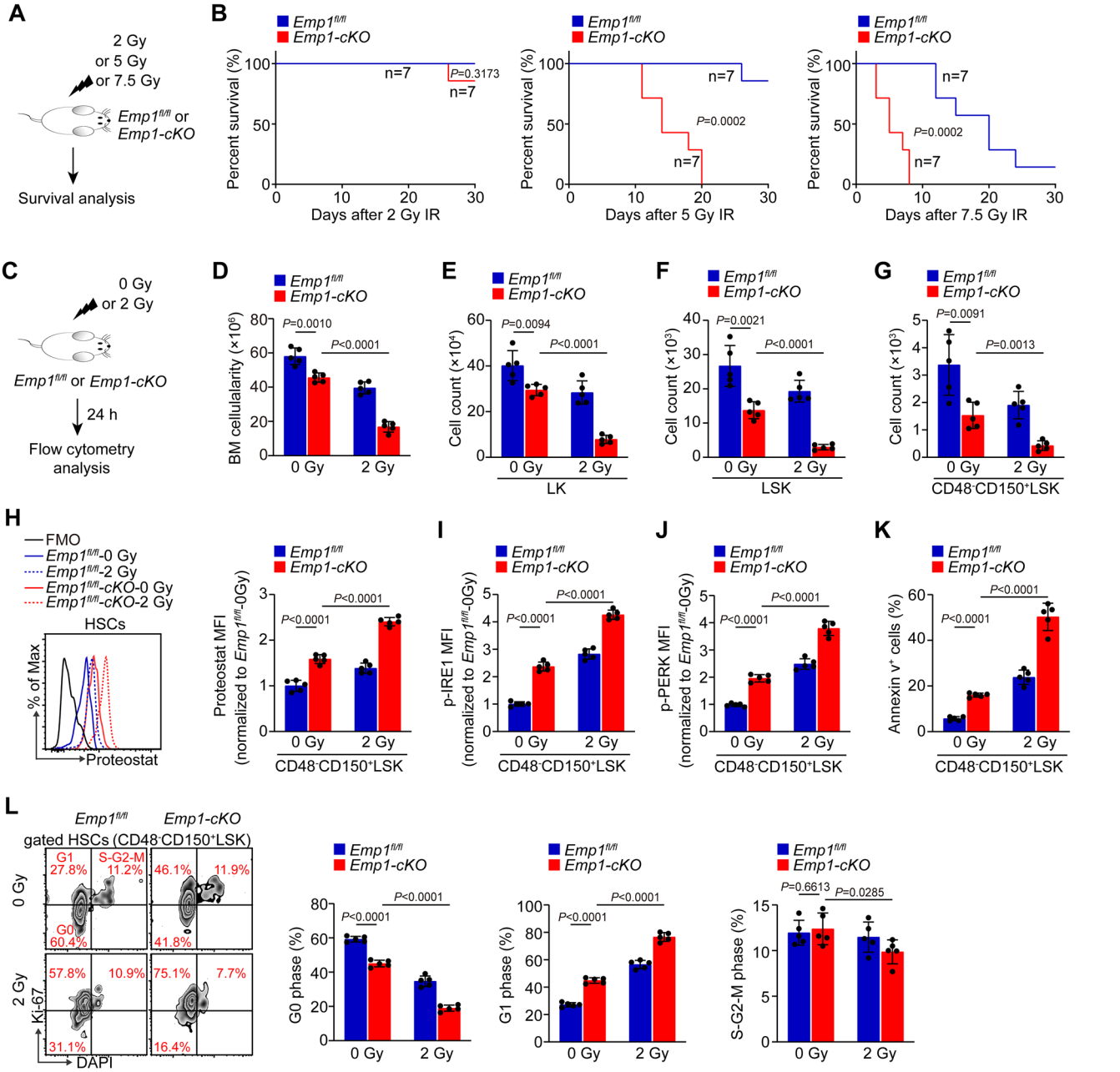

Fig. 5 | Loss of *Emp1* aggravates HSC defects under IR conditions. **A** Experimental schematic. *Emp1*$^{fl/fl}$ and *Emp1-cKO* mice were exposed to various doses (2, 5, or 7.5 Gy) of γ-irradiation. **B** Survival curves of *Emp1*$^{fl/fl}$ and *Emp1-cKO* mice after exposure to γ-irradiation ($n = 7$ mice per group). **C** Experimental schematic. *Emp1*$^{fl/fl}$ and *Emp1-cKO* mice were exposed to a dose of 2 Gy γ-irradiation, followed by flow cytometry analysis. **D**–**G** Graphs represent the cell count of different hematopoietic cell subsets in BM of mice ($n = 5$ mice per group). **H** Flow cytometry analysis of protein aggregate levels in HSCs (CD48$^-$CD150$^+$LSK) using ProteoStat staining. Right graph represents the MFI of ProteoStat in HSCs ($n = 5$ mice per group). **I**, **J** Graphs represent the MFI of p-IRE1 (**I**) and p-PERK (**J**) in HSCs (CD48$^-$CD150$^+$LSK) using flow cytometry staining and analysis ($n = 5$ mice per group). **K** A graph represents the percentages of apoptotic HSCs (CD48$^-$CD150$^+$LSK) ($n = 5$ samples per group). **L** Representative flow plots of the Ki-67 and DAPI staining of HSCs (CD48$^-$CD150$^+$LSK). *Emp1*$^{fl/fl}$ and *Emp1-cKO* mice were exposed to a dose of 2 Gy γ-irradiation, followed by flow cytometry analysis. Right graph represents the percentages of cell-cycle distribution of HSCs ($n = 5$ mice per group). Statistical analyses were performed using log-rank test for 5B; two-tailed unpaired Student's *t*-test for all other analyses. Data are shown as mean ± SD. Results are representative of two independent experiments. Source data are provided as a Source Data file.

this study, we have identified EMP1 as a CERS2 inhibitor through direct binding to the Lag1p domain of CERS2 in murine Lin$^-$c-Kit$^+$ cells, suggesting cell type specificity in terms of CERS2 partners. Moreover, we observed an accumulation of C22–C24-dhCers, which are products generated by CERS2, in HSCs. There are six enzymes in the CERS family, namely CERS1-6, each with a specific preference for the length of acyl-CoA chain used for Cer synthesis[37]. Based on these findings, further assessment is required to determine whether other types of CERS (1, 3–6) and downstream dhCers (C18-C22- and C26-dhCers) impact the protein homeostasis of HSCs.

Preserving and improving the potential of HSCs for clinical use has long been a challenge[58]. Exposure to high doses of IR can induce long-term BM suppression, but there are limited efficient strategies to protect HSCs[25,26]. Increased ER stress has been observed in HSCs during hematopoietic stress[49]. In this study, we have demonstrated that suppressing ER stress efficiently improves HSC potential and

https://doi.org/10.1038/s41467-025-61552-0

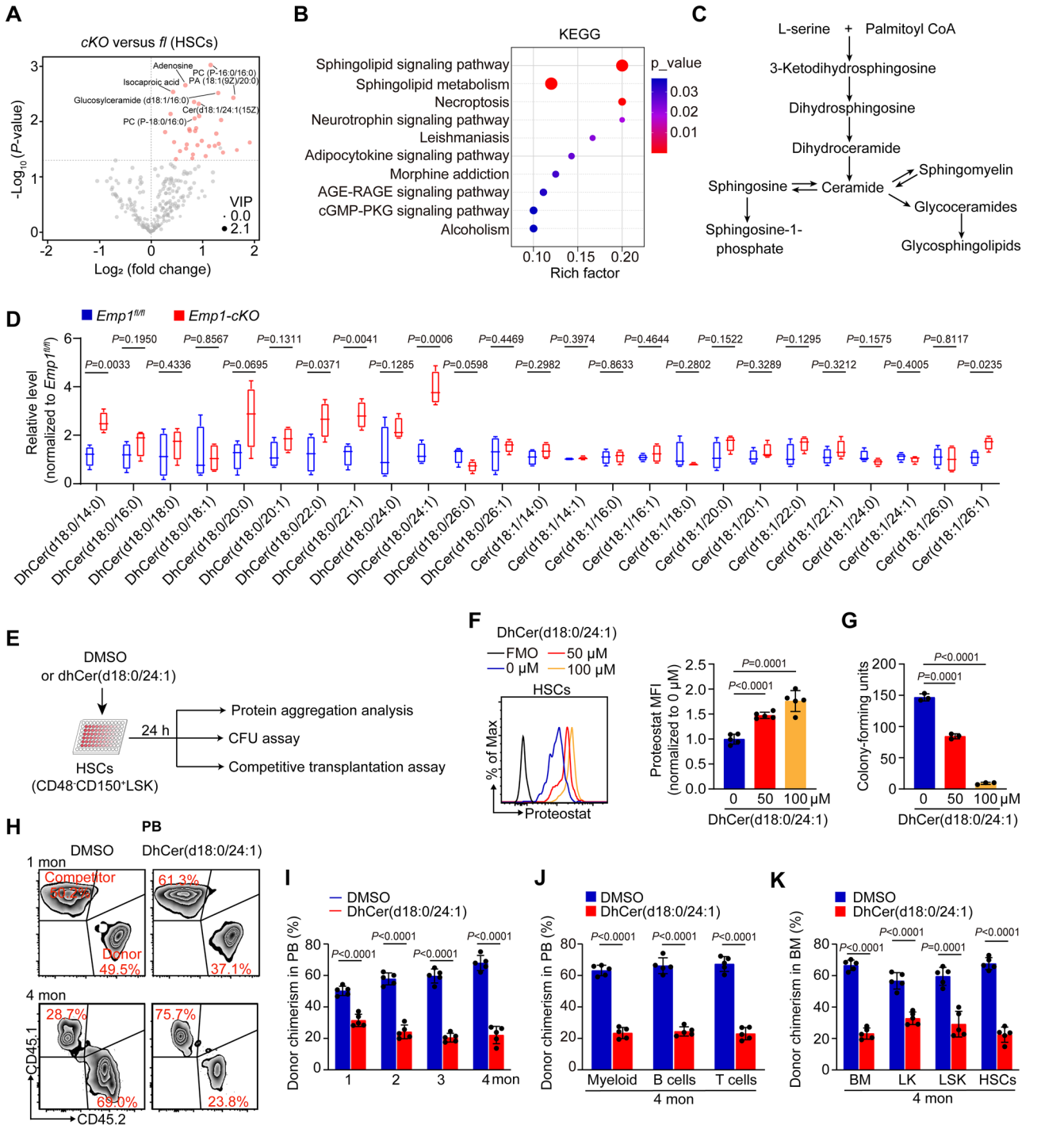

Fig. 6 | *Emp1* deficiency results in dhCer accumulation that induces the formation of protein aggregates. A A representative volcano plot of the metabolite content change between *Emp1*$^{fl/fl}$ and *Emp1-cKO* HSCs (CD48$^-$CD150$^+$LSK) using untargeted metabolomic analysis ($n = 5$ samples per group). All significantly changed metabolites (Variable Importance in the Project [VIP] > 1.0; $p < 0.05$) are indicated by blue or red dots. **B** The KEGG analysis of the enrichment and classification of the significantly changed metabolites. **C** Summary of the sphingolipid metabolism. **D** Relative quantification of dihydroceramide (dhCer) and ceramide (Cer) levels in *Emp1*$^{fl/fl}$ and *Emp1-cKO* HSCs (CD48$^-$CD150$^+$LSK) through lipidomic analysis ($n = 4$ samples per group). The box plot represents the minimum, median, and maximum values. **E** Experimental scheme for the assessment of the impact of dhCer(d18:0/24:1) on HSC function. HSCs (CD48$^-$CD150$^+$LSK) were isolated from *wild-type* C57BL/6J mice and treated with dhCer(d18:0/24:1) for 24 h, followed by flow cytometry analysis, colony-forming unit assay, and competitive transplantation assay. For competitive transplantation assay, 500 HSCs (CD45.2) were mixed with 1.5×10^6 competitor BM cells (CD45.1) and transplanted into recipient mice (CD45.1CD45.2). **F** Flow cytometry analysis of protein aggregate levels in HSCs using ProteoStat staining. Right graph represents the MFI of ProteoStat in HSCs ($n = 5$ samples per group). **G** A graph represents the colony numbers from dhCer-treated HSCs ($n = 3$ samples per group). **H** Representative flow plots of the chimerism of PB from recipients at 1 and 4 months after transplantation. Donor-derived cells, CD45.2$^+$; competitor-derived cells, CD45.1$^+$. **I** The percentages of donor-derived cells in PB at indicated times ($n = 5$ recipients per group). **J** The percentages of donor-derived myeloid cells, B cells, and T cells in PB cells of recipient mice at 4 months after transplantation ($n = 5$ recipients per group). **K** The percentages of donor-derived BM cells, LK, LSK, and HSCs in BM of recipients at 4 months after transplantation ($n = 5$ recipients per group). All statistical analyses were performed using two-tailed unpaired Student's *t*-test. Data are shown as mean ± SD. Results are representative of two independent experiments. Source data are provided as a Source Data file.

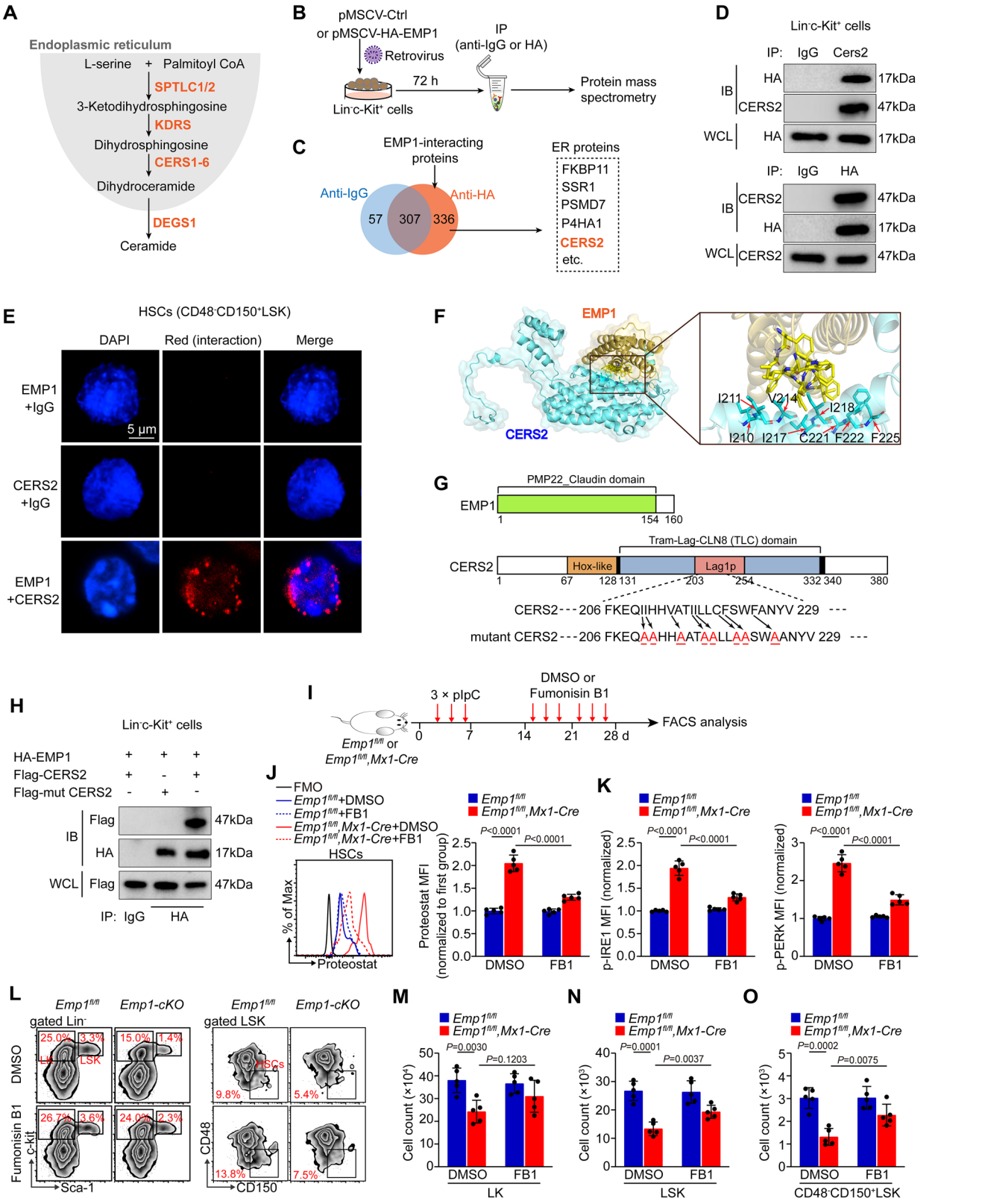

protects HSCs against IR-induced injury. HSCs primarily reside in the BM under hypoxic conditions[8], and in vitro culture and IR often result in ROS production in HSCs[59]. It is possible that elevated ROS levels lead to ER stress in HSCs under in vitro culture and IR conditions. Given that several targets have been identified to preserve HSC function under various conditions[60,61], it is appealing to develop collaborative strategies aimed at enhancing HSC potential, along with EMP1-CERS2 targets.

Methods

Resources

All the reagents and resources, including antibodies, chemicals, and commercial kits, can be found in Supplementary Table 1.

Mice

Wild-type (*WT*), *Emp1*$^{fl/+}$, *Tie2-Cre*, and *Mx1-Cre* were obtained from the Cyagen and on C57BL/6J background (CD45.2). The B6.SJL (CD45.1)

Fig. 7 | EMP1 binds the Lag1p domain of CERS2 to restrict dhCer production. **A** Summary of the pathway of ceramide synthesis. **B** Experimental scheme. BM $Lin^-c\text{-}Kit^+$ cells derived from *wild-type* mice were infected with retrovirus to force EMP1 overexpression (with HA tag). Then IgG or HA antibodies were used to conduct co-immunoprecipitation (co-IP), followed by and mass spectrometry analysis. **C** Venn diagrams represent proteins pulled down by IgG or HA antibodies. **D** The interaction between EMP1 and CERS2. IgG, CERS2, or HA antibodies were used to conducted co-immunoprecipitation (co-IP), followed by immunoblot analysis. Bands representative of two independent experiments with similar results are shown. **E** In situ proximity ligation assay to detect EMP1/CERS2 interaction in murine HSCs ($CD48^-CD150^+LSK$) by utilizing antibodies (rabbit anti-EMP1 and mouse anti-CERS2). Nuclei are stained with DAPI (blue). The scale bar represents 5 μm. **F** Molecular docking of EMP1 (AlphaFold prediction: AF-P47801-F1) and CERS2 (AlphaFold prediction: AF-Q924Z4-F1) using ClusPro2.0 server. **G** Presentation of structure domains of EMP1 and CERS2, along with the design of CERS2 mutations (indicated with red font). **H** The interaction between EMP1 and CERS2 is revealed by co-IP followed by immunoblot analysis. BM $Lin^-c\text{-}Kit^+$ cells were infected with retrovirus to express Flag-CERS2 or Flag-mutant CERS2, together with HA-EMP1 overexpression, followed by co-IP. IgG antibody was used as the negative control. Bands representative of two independent experiments with similar results are shown. **I** Experimental schematic. **J** Flow cytometry analysis of protein aggregate levels in HSCs ($CD48^-CD150^+LSK$) using ProteoStat staining. Right graph represents the MFI of ProteoStat in HSCs ($n = 5$ mice per group). **K** Graphs represent the MFI of p-IRE1 (left) and p-PERK (right) in HSCs ($CD48^-CD150^+LSK$) using flow cytometry staining and analysis ($n = 5$ mice per group). **L** Representative flow plots of the LK ($Lin^-Sca\text{-}1^-c\text{-}Kit^+$), LSK ($Lin^-Sca\text{-}1^+c\text{-}Kit^+$), and HSC ($CD48^-CD150^+LSK$) populations in BM cells from mice. **M**–**O** Graphs represent the cell count of different hematopoietic cell subsets in BM of mice ($n = 5$ mice per group). All statistical analyses were performed using two-tailed unpaired Student's *t*-test. Data are shown as mean ± SD. Results are representative of two independent experiments. Source data are provided as a Source Data file.

were also obtained from the Cyagen. To achieve inducible or tissue-specific deletion of *Emp1*, $Emp1^{fl/fl}$ mice aged 8–12 weeks were crossbred with *Mx1-Cre* or *Tie2-Cre* mice. All genotyping primers are detailed in Supplementary Table 2. The $Emp1^{fl/fl}$, *Mx1-Cre* cohort received polyinosinic:polycytidylic acid (pIpC) (GE Healthcare) injections at a dosage of 10 mg/kg every other day for a total of three administrations to induce Cre recombinase expression. CD45.1CD45.2 mice were generated by the crossbreeding of B6.SJL (CD45.1) mice with C57BL/6J (CD45.2) mice. Age- and sex-matched littermates served as controls for all experimental procedures. All mice utilized in the experiments comprised a mix of both male and female subjects. At the time of experimentation, 10–12-week-old mice were randomly assigned to various experimental groups. All animals were housed under specific pathogen-free conditions and group-housed in a temperature-controlled environment (23 °C) on a 12 h (h) light/dark cycle with *ad libitum* access to standard rodent chow (Keao Xieli Feed Co., Ltd) at the Experimental Animal Center of Chongqing Medical University. The ambient humidity was maintained at 40–60%. All procedures received approval from the Institutional Animal Care and Use Committee at Chongqing Medical University.

Human cord blood CD34+ cells

Human donor samples were obtained with informed consent at the First Affiliated Hospital of Chongqing Medical University in congruence with the protocol approved by the Medical Ethics Committee of Chongqing Medical University (#2025-014). Cord blood samples were subjected to blood cell lysis buffer (Solarbio) to remove red blood cells. Subsequently, hematopoietic progenitor cells were enriched using the EasySep™ Human Progenitor Cell Enrichment Kit II (STEMCELL Technologies). Then the enriched cells were then incubated with an anti-CD34 antibody (BioLegend), followed by sorting of $CD34^+$ cells via flow cytometry.

Cell lines

HEK293T cells were cultured in DMEM (Hyclone), containing 10% FBS (Hyclone) and 1% penicillin/streptomycin (Solarbio).

Primary cell culture

Human cord blood $CD34^+$ cells were cultured in IMDM medium (Hyclone) supplemented with the following components: 10% human serum (Gemini), 1 × penicillin/streptomycin, 100 ng/mL SCF, 20 ng/mL FLT3L, and 10 ng/mL IL-7 (Beyotime). Murine Lin^- cells were enriched using the EasySep™ Mouse Hematopoietic Progenitor Cell Isolation Kit (STEMCELL Technologies). Murine $Lin^-c\text{-}kit^+$ cells, LSK cells ($Lin^-Sca\text{-}1^+c\text{-}kit^+$), and HSCs ($CD48^-CD150^+LSK$) were sorted by flow cytometry. These sorted cells were cultured in IMDM medium supplemented with 10% FBS (STEMCELL Technologies), 1 × penicillin/streptomycin, 0.05 mM 2-mercaptoethanol, 100 ng/mL SCF, 10 ng/mL IL-3, and 10 ng/mL IL-6 (Beyotime).

γ-Irradiation

For cell irradiation, the cells were cultured in 96-well plates and subjected to a single dose of 2 or 5 Gy γ-irradiation using a ^{60}Coγ-ray generator (Radiation Center, Department of Preventive Medicine, Third Military Medical University, China) at approximate dose rates of 92.8-95.5 cGy/min. For mice irradiation, mice were subjected to a single dose of 2, 5, 7.5, or 9 Gy γ-irradiation (whole-body) using a ^{60}Co γ-ray generator at approximate dose rates of 92.8-95.5 cGy/min.

Drug and dhCer treatment

In vitro, HSCs were cultured with azoramide (15 μM, Selleck), tunicamycin (5 μM, MCE) or fumonisin B1 (10 μM, Aladdin) for indicated times. For dhCer treatment, HSCs were cultured with different concentrations of C24:1 Dihydroceramide (d18:0/24:1(15Z)) (Sigma-Aldrich). To induce an acute ER stress in mice, *C57BL/6J* mice were intraperitoneally injected with a dose of tunicamycin (2 mg/kg). For rescue experiments, $Emp1^{fl/fl}$ and $Emp1^{fl/fl}$, *Mx1-Cre* mice were injected with pIpC (10 mg/kg, every other day, thrice) to induce *Emp1* deletion, followed by fumonisin B1 (FB1) injection (2 mg/kg, thrice/week) for two weeks. All the chemical reagents were dissolved in DMSO and their details can be found in Supplementary Table 1.

Plasmids and virus production

To knock down *EMP1*, we designed shRNA oligonucleotides (Supplementary Table 1) and cloned them into the pLKO.1-puro-CMV-GFP vector. For the generation of vectors expressing HA-Emp1, Flag-Cers2, and mutant Cers2, the coding sequences (CDS) were synthesized by Tsingke and then cloned into the pMSCV-GFP vector. HEK293T cells (ATCC, CRL-3216) were utilized for virus production; these cells were transfected with lentiviral or retroviral plasmids along with helper plasmids. Supernatants were collected 48- and 72-h post-transfection, filtered through a 0.22 μm membrane, and concentrated using an Amicon® Ultra-15 10 K (Millipore). For in vitro viral infection of hematopoietic cells, spin infection was performed at 250 g at room temperature for 2 h in the presence of polybrene (8 μg/mL).

Colony-forming unit (CFU) assay

Approximately 100 to 300 HSCs characterized as $CD48^-CD150^+LSK$ were cultured in either 12-well or 6-well culture plates, respectively, using Methylcellulose Complete Media M3434 (STEMCELL Technologies). Following an incubation period of 7 to 10 days, the colonies of granulocytes, erythroid cells, macrophages, and megakaryocytes were enumerated. The cells obtained from the initial culture cycle were subsequently collected and re-seeded into a new culture dish.

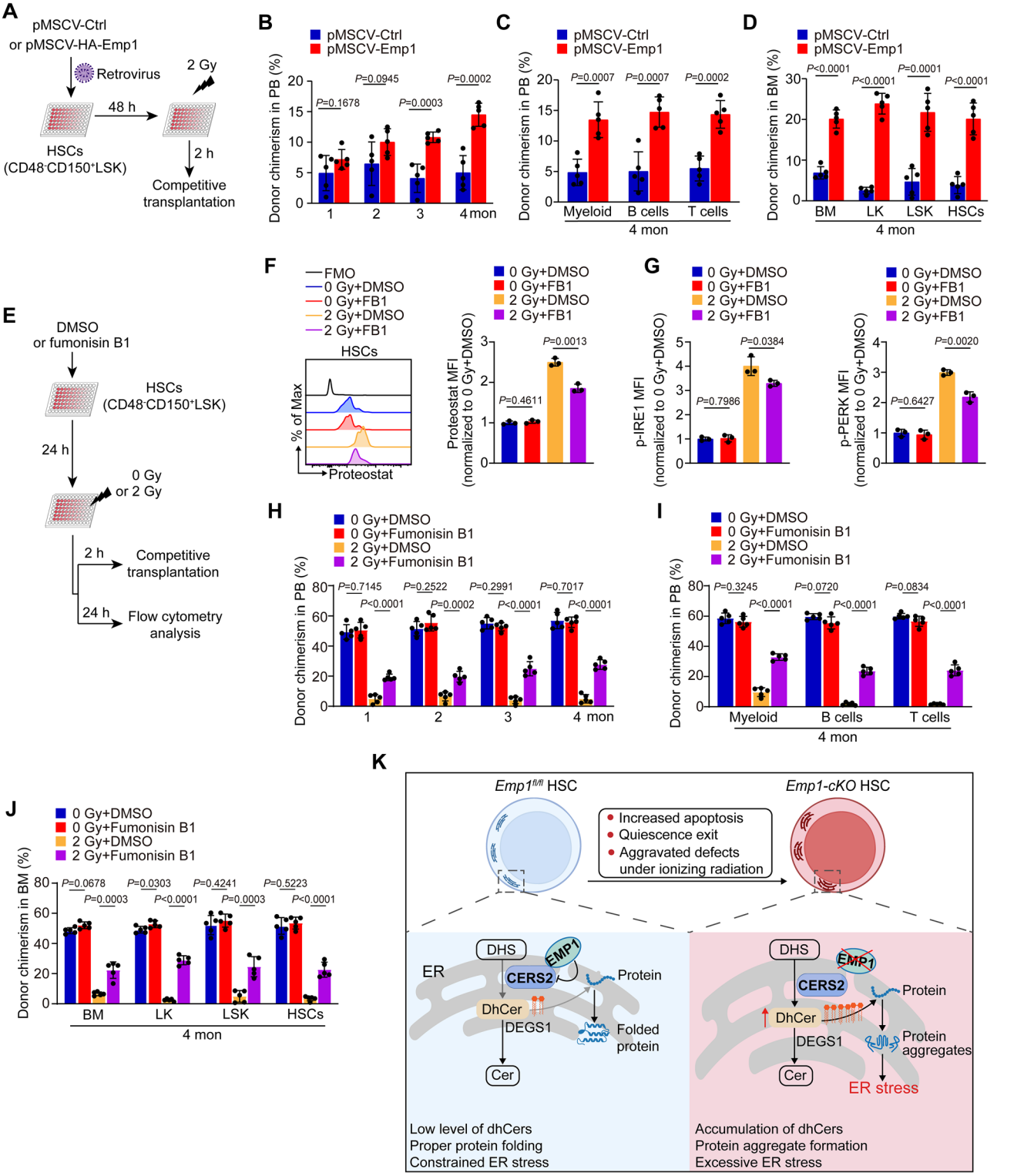

Transplantation assay

For non-competitive transplantation assay, a total of 500 HSCs ($CD48^-CD150^+LSK$) from donor mice (CD45.2) were transplanted into lethally irradiated recipient mice (CD45.1). Two months post-transplantation, the recipient mice were sacrificed for analysis. For the competitive transplantation assay utilizing BM cells, 1.5×10^6 BM cells from *Emp1*$^{fl/fl}$ or *Emp1*$^{fl/fl}$*, Mx1-Cre* mice (CD45.2) were transplanted into lethally irradiated (9.0 Gy) recipient mice (CD45.1), along with 1.5×10^6 competitive BM cells from *wild-type* mice (CD45.1CD45.2). One month post-transplantation, the recipient mice were administered intraperitoneal injections of 10 mg/kg pIpC three times to induce the deletion of *Emp1*. After a duration of four months, 2×10^6 chimeric BM cells from the primary recipients were subsequently transplanted into the second recipient mice. For competitive transplantation assay utilizing HSCs, a total of 500 HSCs ($CD48^-CD150^+LSK$) obtained from donor mice (CD45.2) were mixed with competitor BM cells (1.5×10^6) from *wild-type* mice (CD45.1CD45.2), and this mixture was then transplanted into lethally irradiated (9.0 Gy) recipient mice (CD45.1). After a duration of four months, 2×10^6 chimeric BM cells from the primary recipients were transplanted into the second recipient mice.

Fig. 8 | *Emp1* overexpression or CERS2 inhibition protects HSCs against IR-induced injury. A Experimental schematic. HSCs from *wild-type* C57BL/6J mice were infected with retrovirus to force *Emp1* overexpression, followed by a dose of 2 Gy γ-irradiation. Two hours after radiation exposure, a competitive transplantation assay was conducted in which IR-treated HSCs were used. **B** The percentages of donor-derived cells in PB at indicated times ($n = 5$ recipients per group). **C** The percentages of donor-derived myeloid cells, B cells, and T cells in PB cells of recipient mice at 4 months after transplantation ($n = 5$ recipients per group). **D** The percentages of donor-derived BM cells, LK, LSK, and HSCs in BM of recipients at 4 months after transplantation ($n = 5$ recipients per group). **E** Experimental scheme. HSCs from *wild-type* C57BL/6J mice were treated with DMSO or fumonisin B1 (10 μM) for 24 h, followed by a dose of 2 Gy γ-irradiation. Two hours after radiation exposure, a competitive transplantation assay was conducted in which IR-treated HSCs were used. Additionally, another group of HSCs was cultured for 24 h post-irradiation, followed by flow cytometry analysis. **F** Flow cytometry analysis of protein aggregate levels in HSCs ($CD48^-CD150^+LSK$) using ProteoStat staining. Right graph represents the MFI of ProteoStat in HSCs ($n = 5$ mice per group). **G** Graphs represent the MFI of p-IRE1 (left) and p-PERK (right) in HSCs ($CD48^-CD150^+LSK$) using flow cytometry staining and analysis ($n = 5$ mice per group). **H** The percentages of donor-derived cells in PB at indicated times ($n = 5$ recipients per group). **I** The percentages of donor-derived myeloid cells, B cells, and T cells in PB cells of recipient mice at 4 months after transplantation ($n = 5$ recipients per group). **J** The percentages of donor-derived BM cells, LK, LSK, and HSCs in BM of recipients at 4 months after transplantation ($n = 5$ recipients per group). **K** A proposed model scheme represents the roles and molecular mechanisms of EMP1 safeguarding HSCs via CERS2-mediated sphingolipid metabolism. All statistical analyses were performed using two-tailed unpaired Student's *t*-test. Data are shown as mean ± SD. Results are representative of two independent experiments. Source data are provided as a Source Data file.

The chimerism was analyzed monthly using anti-mouse CD45.1 and anti-mouse CD45.2 antibodies, along with various cell surface markers.

In vivo limiting dilution assay

5×10^3, 1×10^4, 5×10^4, and 1×10^5 BM cells from *Emp1*$^{fl/fl}$ or *Emp1*$^{fl/fl}$,*Tie2-Cre* mice (CD45.2) were transplanted into lethally irradiated CD45.1 mice, along with 5×10^5 competing BM cells from CD45.1CD45.2 mice. A cell dose was considered to contain at least one competitive repopulation unit if donor engraftment in the BM of recipient mice exceeded 1% of both lymphoid and myeloid lineages at 12 weeks post-transplantation. Extreme limiting dilution analysis is a coherent approach to limiting dilution analysis which includes extreme data situations, multiple populations and non-Poisson situations[62]. The HSC frequency was calculated and the log-fraction plot was generated using extreme limiting dilution analysis (https://bioinf.wehi.edu.au/software/elda/).

Flow cytometric analysis and cell sorting

All utilized antibodies can be found in the Supplementary Table 1. Cell suspensions from PB, spleen, thymus, and BM were harvested. To analyze myeloid differentiation, cells were stained with fluorescent dye-labeled antibodies, including antibodies anti-Gr-1, anti-Mac, anti-Ter119, anti-CD71, anti-IgM, anti-B220, anti-CD8a, and anti-CD4. When analyzing HSPCs, staining with biotin-conjugated antibodies (lineage antibodies) was performed, followed by staining with anti-Streptavidin-PE/Cyanamide5 and fluorescent dye-labeled antibodies. The following are cell surface markers for different populations: Lin^- cells ($Gr\text{-}1^-Ter119^-B220^-CD19^-$Rat $IgM^-IL\text{-}7R^-CD3\varepsilon^-$), LK cells ($Lin^-Sca\text{-}1^-c\text{-}kit^+$), LSK cells ($Lin^-Sca\text{-}1^+c\text{-}kit^+$), ST-HSCs ($CD34^+CD135^-LSK$), HSCs ($CD48^-CD150^+LSK$ or $CD34^-CD135^-LSK$), MPP ($CD34^+CD135^+LSK$), LMPP ($CD135^{high}LSK$), CMP ($Lin^-Sca\text{-}1^-c\text{-}kit^+CD16/32^{med}CD34^+$), GMP ($Lin^-Sca\text{-}1^-c\text{-}kit^+CD16/32^+CD34^+$), and MEP ($Lin^-Sca\text{-}1^-c\text{-}kit^+CD16/32^-CD34^-$). The characterization of cell populations can be found in the Supplementary Table 3. Flow cytometric detection was conducted using a BD FACS Canto II (BD Biosciences), and all data were analyzed using FlowJo 10.0 Software (TreeStar). Cell sorting was performed using a BD FACS Aria^{TM}III (BD Biosciences).

5-FU treatment

5-FU (150 mg/kg, Sigma) was administered to mice via intraperitoneal injection once a week for a duration of three weeks. The survival of each individual mouse was monitored daily.

Cell cycle and apoptosis analysis

All utilized antibodies can be found in the Supplementary Table 1. For the cell cycle analysis of HSCs, BM cells were harvested from mice, labeled with specific cell surface markers as previously described, and subsequently fixed and permeabilized using the Cytofix/Cytoperm™ Fixation/Permeabilization Kit (BD Biosciences). HSCs were then stained with Ki-67 FITC (1:50) and DAPI (5 μg/mL), followed by flow cytometric analysis. For apoptosis assessment of HSCs, BM cells from mice were collected, stained with cell surface markers, and subsequently treated with Annexin-V APC (1:20) and DAPI (0.5 μg/mL), followed by flow cytometric analysis.

Quantification of aggregated proteins

The aggregated protein levels of HSCs were analyzed using the ProteoStat Staining Kit (Enzo Life Sciences). The ProteoStat dye functions as a molecular rotor. In solution, free intramolecular rotation along a single central bond prevents fluorescence. The ProteoStat dye specifically intercalates into the cross-beta spine of quaternary protein structures typically found in misfolded and aggregated proteins, which will inhibit the dye's rotation and lead to a strong fluorescence. BM cells from mice were collected and stained with cell surface markers as previously described. Subsequently, fixation and permeabilization were performed using the Cytofix/Cytoperm™ Fixation/Permeabilization Kit (554714, BD Biosciences), following the manufacturer's instructions. Fixed cells were then stained with a 1:10,000 dilution of ProteoStat dye in permeabilization solution for 30 min. Then, the cells were washed with FACS buffer prior to flow cytometric analysis.

RNA extraction and quantitative RT-PCR (qRT-PCR) analysis

Total RNA was extracted from FACS-sorted cells using an miRNeasy Mini Kit (QIAGEN) according to the manufacturer's instructions. Then, total RNA was reverse transcribed using the PrimeScript^{TM} RT reagent Kit with gDNA Eraser (Takara). PCR reactions were conducted using 2× Universal SYBR Green Fast qPCR Mix (Takara). The relative expression of each gene was normalized to actin and quantified using the $2^{-\Delta\Delta CT}$ methods. Each reaction was performed in triplicate. Primer sequences are provided in Supplementary Table 2.

Immunoprecipitation assays and western blot

Immunoprecipitation was conducted utilizing the Immunoprecipitation Kit with Protein A + G Agarose Gel (Beyotime). The products obtained from co-immunoprecipitation were subsequently analyzed through proteomics and western blotting. For the western blot analysis, cells were lysed using RIPA lysis buffer (1× PBS, 1% NP-40, 0.1% SDS, 0.5% sodium deoxycholate, 1 mM EDTA), and the resulting protein extracts were subjected to electrophoresis on polyacrylamide gels before being transferred to nitrocellulose membranes. Following a one-hour incubation in blocking buffer at room temperature, the membranes were incubated overnight at 4 °C with the appropriate antibodies. The antibodies employed in this study are detailed in Supplementary Table 1. All antibodies were utilized at a dilution ratio of 1:1000. The HRP-conjugated secondary antibodies used included goat anti-rabbit or goat anti-mouse (dilution of 1:1000). The ER was isolated using a Reagent Kit for Protein Extraction from the ER (Solarbio), in accordance with the manufacturer's instructions.

Immunofluorescence assay

The HSCs ($CD48^-CD150^+LSK$) were sorted and evenly spread on a glass slide coated with poly-lysine, followed by fixed with 4% paraformaldehyde (PFA) at room temperature for 30 min, permeabilized with 0.1% Triton X-100 for 5 min, and blocked with 5% goat serum at room temperature for 1 h. Dilutions of anti-Emp1 (bs-0558R, Bioss) and anti-Calreticulin (A27115, Abclonal) antibodies were prepared in accordance with the manufacturer's instructions using 5% goat serum. These dilutions were then applied to the glass slide and incubated overnight at 4 °C. Then the slides were incubated with secondary antibodies conjugated to ABflo®488 (AS053, Abclonal) and ABflo®594 (AS054, Abclonal). The cell nuclei were stained with DAPI (D8417, Sigma-Aldrich), after which they were analyzed using fluorescence microscopy.

Dulink proximity ligation assay (PLA)

Duolink PLA was performed according to the manufacturer's instructions (DUO92101, Sigma-Aldrich). The HSC suspension obtained by sorting was evenly spread on a glass slide coated with poly-lysine, fixed with 4% PFA at room temperature for 20 min, permeabilized with 0.1% Triton X-100 for 5 min. Cells were then blocked in 5% BSA and incubated with primary antibodies (rabbit anti-EMP1 and mouse anti-CERS2). After washing the cells, PLA probes were added, followed by hybridization, ligation, and amplification for 90 min at 37 °C. Finally, cells were incubated with the detection solution and visualized by fluorescence microscopy.

Molecular docking

The three-dimensional structure PDB files of EMP1 (AF-P47801-F1 predicted by AlphaFold) and CERS2 (AF-Q924Z4-F1 predicted by AlphaFold) were submitted to the ClusPro 2.0 server for protein-protein docking prediction. The optimal model was selected from the predicted results and displayed using the molecular visualization tool PyMOL 2.6.

scRNA-seq data analysis

The scRNA-seq datasets of BM cells derived from five healthy donors, with associated cell annotation information, were collected from the Gene Expression Omnibus (GEO) database (GSE116256)[31]. R package Seurat (version 5.0.1) was employed for clustering and differential expression analysis was conducted with the built-in FindMarkers function.

RNA-seq and data analysis

HSCs ($CD48^-CD150^+LSK$) were directly sorted into TRIzol-LS (Thermo Fisher Scientific), at a density of approximately 500–1000 cells per sample[63]. Total RNA was extracted using the miRNeasy kit (QIAGEN). The mRNA was reverse transcribed and amplified following the Geo-seq method, and the library was constructed using the TruePrep DNA Library Preparation Kit V2 (Vazyme) according to the manufacturer's instructions. The library was sequenced using the Illumina NovaSeq 6000 platform, with sequencing comprising 150-bp of paired-end reads. For data processing, RNA-seq reads were aligned to the mm10 using Hisat2. Aligned reads were counted with HTSeq (a Python framework to work with high-throughput sequencing data). Fragments per kilobase per million estimation was performed with Cufflinks v2.1.1. Differential expression analysis was performed with limma-voom pipeline in R. Differentially expressed genes were selected using a cutoff P value of <0.05 (false discovery rate adjusted for multiple testing). The volcano of gene expression was plotted using R. GSEA was performed using GSEA software (v4.1.0) (http://www.broadinstitute.org/gsea) with 1000 permutations.

ATAC-sequence and data processing

Briefly, approximately 5000 HSCs ($CD48^-CD150^+LSK$) were sorted into EP tubes and kept on ice. The cells were lysed with a lysis buffer prepared as follows: 10 mM Tris-HCl, 10 mM NaCl, 3 mM $MgCl_2$, and 0.1% IGEPAL CA-630[63]. The nuclei were collected following centrifugation at 4 °C. The DNA fragmentation mix was prepared according to the instructions provided with the Novoprotein Chromatin Profile Kit for Illumina (Novoprotein). The reaction was conducted using a PCR instrument at 37 °C for 30 min, after which the DNA fragmentation products were recovered and purified. PCR amplification was performed following the instructions provided with the Novoprotein NovoNGS® Index Kit for Illumina® (Novoprotein). The number of amplification cycles was precisely adjusted based on the cell number. The PCR products were subsequently purified and recovered using Novoprotein DNA Clean Beads (Novoprotein). Finally, the library concentration was assessed using Qubit (Thermo Fisher Scientific), and the library distribution was evaluated using the Agilent 2100. Libraries were sequenced by the Illumina NovaSeq 6000 platform as 150-bp pair-ended reads.

For data processing, low-quality reads and adaptor sequences were removed by Trim Galore v0.4.4 with parameters "-q 10 -length 30 -stringency 5"". Paired-end reads were mapped to the mm10 reference genome using BWA. Reads that aligned to the mitochondrial genome were filtered, and PCR duplicates were removed with sambamba-markdup. To identify peaks, the bam files containing unique, nonchrM reads were used to call peaks with MACS2 using parameters "–nomodel–shift-100–extsize 200". For differential coverage, corresponding bam files were merged to call peaks to get a union peak set. For each peak in the peak set, raw ATACseq reads were counted by featureCounts. Differentially expressed peaks were identified by at least a 1.5-fold change and false discovery rate adjusted P value of 0.01. The deepTools compute matrix (reference point) function was used to calculate the ATAC signal and create heat maps; the volcano of differentially expressed peaks and violin plots of the ATAC signal (log2(normalized RPKM)) at specified regions were plotted using R. A Student's t-test was used to test the significance. The Integrative Genomics Viewer tool was used for visualizing the ATAC-seq data.

UHPLC-MS/MS-based untargeted metabolomics

For untargeted metabolomics, approximately 50,000 HSCs ($CD48^-CD150^+LSK$) were sorted and were rapidly frozen in liquid nitrogen for 30 s and stored at −80 °C until use. The UHPLC-MS/MS-based untargeted metabolomics analysis was conducted by BIOTREE Biomedical Technology (Shanghai, China). An extract solution of 1000 µL (methanol: acetonitrile: water = 2:2:1, containing an isotopically labeled internal standard mixture) was added to the samples. Subsequently, the samples underwent three freeze-thaw cycles using liquid nitrogen. They were then sonicated for 10 min in an ice-water bath. Following this step, the samples were incubated for one hour at −40 °C and centrifuged at 10,000 × g for 15 min at a temperature of 4 °C. The resulting supernatant was transferred to a fresh glass vial for subsequent analysis. LC-MS/MS analyses were performed utilizing a Vanquish UHPLC system (Thermo Fisher Scientific), equipped with a UPLC BEH Amide column (2.1 mm × 100 mm; particle size: 1.7 µm), coupled to an Orbitrap Exploris 120 mass spectrometer (Thermo Fisher Scientific). The mobile phase comprised of aqueous solutions containing ammonium acetate and ammonia hydroxide at a concentration of 25 mmol/L each (pH = 9.75) as component A and acetonitrile as component B. The auto-sampler temperature was maintained at 4 °C with an injection volume set to 2 µL. MS/MS spectra were acquired on information-dependent acquisition mode in the acquisition software (Xcalibur, version 4.2 SP1). ESI source conditions were established as follows: sheath gas flow rate set to 50 Arb; auxiliary gas flow rate set to 15 Arb; capillary temperature maintained at 320 °C; full MS resolution configured at 60,000; MS/MS resolution set to 15,000; collision energy adjusted to 10/30/60 in NCE mode; spray voltage applied at 3.8 kV (for positive ionization) or −3.4 kV (for negative ionization), respectively.

The raw data were converted to the mzXML format using ProteoWizard and subsequently processed with an in-house program developed in R, which is based on XCMS for peak detection, extraction, alignment, and integration. An internal MS2 database (BiotreeDB) was utilized for metabolite annotation. In this study, 7388 peaks were detected and 7381 metabolites were left after relative standard deviation de-noising. An internal standard normalization method was utilized in the analysis of this data. The final dataset, as detailed in Supplementary Data 1, which includes the sample names and normalized peak areas, was imported to SIMCA16.0.2 software package for multivariate analysis. Metabolites with MS/MS matching score (MS2 score) > 0.3 were included for subsequent analysis, with a total of 283 annotated MS/MS metabolites. To visualize group separation and find significantly changed metabolites, orthogonal projections to latent structures-discriminant analysis (OPLS-DA) were conducted using a permutation test in SIMCA 16.0.2 software. The value of variable importance in the projection (VIP) of the first principal component in OPLS-DA analysis was obtained. The metabolites with VIP > 1 and $p < 0.05$ (Student's t-test) were considered as significantly changed metabolites. In addition, commercial databases including KEGG and MetaboAnalyst (http://www.metaboanalyst.ca/) were used for pathway enrichment analysis.

UHPLC-MS/MS-based lipidomics

For lipidomics, approximately 500,000 HSCs ($CD48^{-}CD150^{+}LSK$) were sorted and were rapidly frozen in liquid nitrogen for 30 s and stored at −80 °C until use. The UHPLC-MS/MS-based lipidomics was performed by BIOTREE Biomedical Technology (Shanghai, China). The entire cell sample was mixed with 200 µL of water and vortexed for 60 s. The samples underwent three freeze-thaw cycles using liquid nitrogen, followed by sonication in an ice-water bath for 20 min. Subsequently, the homogenate (200 µL) was combined with 480 µL of extraction solution (MTBE: MeOH = 5:1), which contained the internal standard. After vortexing for an additional 60 s, the samples were sonicated again for 10 min in an ice-water bath. Next, the samples were centrifuged at 2000 × g for 15 min at a temperature of 4 °C. A volume of 250 µL of supernatant was transferred to a fresh tube. The remaining sample received an addition of another 250 µL of MTBE, followed by vortexing, sonication, and centrifugation; another aliquot of 250 µL supernatant was then collected. This step was repeated once more. The combined supernatants were concentrated under vacuum at a temperature of 37 °C until dry. The dried residues were subsequently reconstituted in 80 µL of resuspension buffer (DCM: MeOH: H_2O = 60:30:4.5). Following this, the samples were vortexed for approximately 30 s and subjected to sonication in an ice-water bath for another ten minutes. Finally, the resulting suspension was centrifuged at a speed of 10,000 × g for fifteen minutes at a temperature of four degrees Celsius; thereafter, a volume of thirty-five microliters from the supernatant was transferred into a fresh glass vial for LC/MS analysis.

The UHPLC separation was performed using an ACQUITY Premier series UHPLC System (Waters). The mobile phase A comprised 40% water, 60% acetonitrile, and 10 mmol/L ammonium formate. Mobile phase B consisted of 10% acetonitrile, 90% isopropanol, and 10 mmol/L ammonium formate. The column temperature was maintained at 45 °C. The auto-sampler temperature was set to 10 °C, with an injection volume of 2 µL. For assay development, a Triple Quad™ 6500+ mass spectrometer (SCIEX) was utilized. Typical ion source parameters included: IonSpray Voltage: +5500/−4500 V; Curtain Gas: 40 psi; Temperature: 350 °C; Ion Source Gas 1:50 psi; Ion Source Gas 2:50 psi; DP: ±80 V. Biobud-v2.1.4.1 software was employed for the quantification of the target compounds. The absolute content of individual lipids was calculated based on peak area and the actual concentration of the identical lipid class internal standard (IS), as detailed in Supplementary Data 2.

UHPLC-MS/MS-based proteomics

UHPLC-MS/MS-based proteomics was performed by PTM BIO (Hangzhou, China). In brief, each protein sample was taken in equal amounts for enzymatic digestion. The volume was adjusted to be consistent using lysis buffer, followed by the addition of dithiothreitol (DTT) to achieve a final concentration of 5 mM. The mixture was then reduced at 56 °C for 30 min. Subsequently, iodoacetamide (IAA) was added to reach a final concentration of 11 mM, and the solution was incubated at room temperature in the dark for 15 min. TEAB was used to dilute urea, ensuring that its concentration remained below 2 M. Trypsin was added at a ratio of 1:50 (protease:protein, w/w) for overnight digestion. Afterward, trypsin was again added at a ratio of 1:100 (protease:protein, w/w), and digestion continued for an additional 4 h. The peptide segments were dissolved in mobile phase A and separated using the EASY-nLC 1000 UHPLC system (Thermo Fisher Scientific). After separation by the UHPLC system, the peptides were injected into the NSI ion source for ionization before being analyzed by Q Exactive Plus mass spectrometry (Thermo Fisher Scientific). The ion source voltage was set at 2100 V, allowing for detection and analysis of both precursor ions and their secondary fragments using high-resolution Orbitrap technology. The scanning range for primary mass spectrometry was established between 350 and 1600 m/z with a scanning resolution set at 70,000. The secondary scan resolution was configured at 17,500. Data acquisition utilized data-dependent acquisition (DDA) mode whereby after each primary scan, the top ten precursor ions exhibiting the highest signal intensity were sequentially directed into the HCD collision cell utilizing 28% fragmentation energy for dissociation followed by subsequent secondary mass spectrometric analysis.

The raw data obtained from the mass spectrometer were processed using MaxQuant search engine (v.1.6.15.0). The search parameters were configured as follows: the database used was Mus_musculus_10090_SP_20230103.fasta, containing 17,132 sequences. The tolerances for precursor ion mass error during First Search and Main Search were set at 20 ppm and 4.5 ppm, respectively, while fragment ion mass error tolerance was also maintained at 20 ppm. Carbamidomethyl on Cys was specified as fixed modification, and acetylation on protein N-terminal and oxidation on Met were specified as variable modifications. FDR was adjusted to <1%. To qualify as identified proteins, each must contain at least one unique peptide segment.

Statistics and reproducibility

All experiments included at least three biological replicates. Comparisons between two groups were analyzed using a two-tailed unpaired Student's t-test. The Cox–Mantel test was used to compare two survival curves. Values of $p < 0.05$ were considered statistically significant. All data are means ± SD. No statistical method was used to predetermine the sample size. No data were excluded from the analyses. Blinding was not applicable to this study. Statistical analyses were performed using GraphPad Prism9.5 or Microsoft Excel.

Reporting summary

Further information on research design is available in the Nature Portfolio Reporting Summary linked to this article.

Data availability

All data supporting the findings of this study are available in the article and its Source Data, or from the corresponding authors upon request. RNA-seq and ATAC-seq data have been deposited in the National Center for Biotechnology Information GEO database under accession number GSE277445. Proteomics data have been deposited in the PRIDE-Proteomics Identification Database under accession number PXD055884. Metabolomics data have

been deposited in the MetaboLights under accession numbers MTBLS12489 and MTBLS12491. Source data are provided with this paper.

Code availability

This paper does not contain original code.

References

1. Eaves, C. J. Hematopoietic stem cells: concepts, definitions, and the new reality. *Blood* **125**, 2605–2613 (2015).
2. Dzierzak, E. & Bigas, A. Blood development: hematopoietic stem cell dependence and independence. *Cell Stem Cell* **22**, 639–651 (2018).
3. Kalaitzidis, D. et al. Amino acid-insensitive mTORC1 regulation enables nutritional stress resilience in hematopoietic stem cells. *J. Clin. Invest.* **127**, 1405–1413 (2017).
4. Cabezas-Wallscheid, N. et al. Vitamin A-retinoic acid signaling regulates hematopoietic stem cell dormancy. *Cell* **169**, 807–823.e819 (2017).
5. Van Galen, P. et al. The unfolded protein response governs integrity of the haematopoietic stem-cell pool during stress. *Nature* **510**, 268–272 (2014).
6. Jacobs, K. et al. Stress-triggered hematopoietic stem cell proliferation relies on PrimPol-mediated repriming. *Mol. Cell* **82**, 4176–4188.e4178 (2022).
7. Flach, J. et al. Replication stress is a potent driver of functional decline in ageing haematopoietic stem cells. *Nature* **512**, 198–202 (2014).
8. Chen, Z., Guo, Q., Song, G. & Hou, Y. Molecular regulation of hematopoietic stem cell quiescence. *Cell Mol. Life Sci.* **79**, 218 (2022).
9. Schwarz, D. S. & Blower, M. D. The endoplasmic reticulum: structure, function and response to cellular signaling. *Cell Mol. Life Sci.* **73**, 79–94 (2016).
10. Rellmann, Y., Eidhof, E. & Dreier, R. Review: ER stress-induced cell death in osteoarthritic cartilage. *Cell Signal* **78**, 109880 (2021).
11. Luchsinger, L. L. Hormetic endoplasmic reticulum stress in hematopoietic stem cells. *Curr. Opin. Hematol.* **28**, 417–423 (2021).
12. Liu, L. et al. Adaptive endoplasmic reticulum stress signalling via IRE1α-XBP1 preserves self-renewal of haematopoietic and pre-leukaemic stem cells. *Nat. Cell Biol.* **21**, 328–337 (2019).
13. Xu, L. et al. Protein quality control through endoplasmic reticulum-associated degradation maintains haematopoietic stem cell identity and niche interactions. *Nat. Cell Biol.* **22**, 1162–1169 (2020).
14. Barton, B. M. et al. IRE1α-XBP1 safeguards hematopoietic stem and progenitor cells by restricting pro-leukemogenic gene programs. *Nat. Immunol.* **26**, 200–214 (2025).
15. Sigurdsson, V. et al. Bile acids protect expanding hematopoietic stem cells from unfolded protein stress in fetal Liver. *Cell Stem Cell* **18**, 522–532 (2016).
16. Wang, Y. W., Cheng, H. L., Ding, Y. R., Chou, L. H. & Chow, N. H. EMP1, EMP 2, and EMP3 as novel therapeutic targets in human cancer. *Biochim. Biophys. Acta Rev. Cancer* **1868**, 199–211 (2017).
17. Cañellas-Socias, A. et al. Metastatic recurrence in colorectal cancer arises from residual EMP1^{+} cells. *Nature* **611**, 603–613 (2022).
18. Wang, Y. H. et al. A 4-gene leukemic stem cell score can independently predict the prognosis of myelodysplastic syndrome patients. *Blood Adv.* **4**, 644–654 (2020).
19. Lin, S. Y. et al. A 6-membrane protein gene score for prognostic prediction of cytogenetically normal acute myeloid leukemia in multiple cohorts. *J. Cancer* **11**, 251–259 (2020).
20. Ng, S. W. et al. A 17-gene stemness score for rapid determination of risk in acute leukaemia. *Nature* **540**, 433–437 (2016).
21. Wang, Y. et al. Tunicamycin induces ER stress and inhibits tumorigenesis of head and neck cancer cells by inhibiting N-glycosylation. *Am. J. Transl. Res.* **12**, 541–550 (2020).
22. Pietras, E. M. et al. Functionally distinct subsets of lineage-biased multipotent progenitors control blood production in normal and regenerative conditions. *Cell Stem Cell* **17**, 35–46 (2015).
23. Mercier, F. E., Sykes, D. B. & Scadden, D. T. Single targeted exon mutation creates a true congenic mouse for competitive hematopoietic stem cell transplantation: the C57BL/6-CD45.1(STEM) mouse. *Stem Cell Rep.* **6**, 985–992 (2016).
24. Zhang, Y. et al. Insights into ionizing radiation-induced bone marrow hematopoietic stem cell injury. *Stem Cell Res. Ther.* **15**, 222 (2024).
25. Yang, L. et al. Oxymatrine boosts hematopoietic regeneration by modulating MAPK/ERK phosphorylation after irradiation-induced hematopoietic injury. *Exp. Cell Res.* **427**, 113603 (2023).
26. Zhang, L. et al. Ripk3 signaling regulates HSCs during stress and represses radiation-induced leukemia in mice. *Stem Cell Rep.* **17**, 1428–1441 (2022).
27. Chalot, M. et al. Deleterious effect of bone marrow-resident macrophages on hematopoietic stem cells in response to total body irradiation. *Blood Adv.* **6**, 1766–1779 (2022).
28. Wang, N. et al. TWIST1 preserves hematopoietic stem cell function via the CACNA1B/Ca2+/mitochondria axis. *Blood* **137**, 2907–2919 (2021).
29. Ney, G. M. et al. Oncogenic N-Ras mitigates oxidative stress-induced apoptosis of hematopoietic Stem Cells. *Cancer Res.* **81**, 1240–1251 (2021).
30. Métais, J. Y. et al. BCL2A1a over-expression in murine hematopoietic stem and progenitor cells decreases apoptosis and results in hematopoietic transformation. *PLoS ONE* **7**, e48267 (2012).
31. van Galen, P. et al. Single-cell RNA-seq reveals AML hierarchies relevant to disease progression and immunity. *Cell* **176**, 1265–1281.e1224 (2019).
32. Blais, A. & Dynlacht, B. D. E2F-associated chromatin modifiers and cell cycle control. *Curr. Opin. Cell Biol.* **19**, 658–662 (2007).
33. Nishitoh, H. CHOP is a multifunctional transcription factor in the ER stress response. *J. Biochem.* **151**, 217–219 (2012).
34. Gubas, A. & Dikic, I. ER remodeling via ER-phagy. *Mol. Cell* **82**, 1492–1500 (2022).
35. Gallardo, P., Salas-Pino, S. & Daga, R. R. Reversible protein aggregation as cytoprotective mechanism against heat stress. *Curr. Genet.* **67**, 849–855 (2021).
36. Green, C. D., Maceyka, M., Cowart, L. A. & Spiegel, S. Sphingolipids in metabolic disease: the good, the bad, and the unknown. *Cell Metab.* **33**, 1293–1306 (2021).
37. Hannun, Y. A. & Obeid, L. M. Sphingolipids and their metabolism in physiology and disease. *Nat. Rev. Mol. Cell Biol.* **19**, 175–191 (2018).
38. Parthibane, V. et al. Sptlc1 is essential for myeloid differentiation and hematopoietic homeostasis. *Blood Adv.* **3**, 3635–3649 (2019).
39. Zhaliazka, K., Serada, V., Matveyenka, M., Rizevsky, S. & Kurouski, D. Protein-to-lipid ratio uniquely changes the rate of lysozyme aggregation but does not significantly alter toxicity of mature protein aggregates. *Biochim. Biophys. Acta Mol. Cell Biol. Lipids* **1868**, 159305 (2023).
40. Quinville, B. M., Deschenes, N. M., Ryckman, A. E. & Walia, J. S. A comprehensive review: sphingolipid metabolism and implications of disruption in sphingolipid homeostasis. Int. J. Mol. Sci. **22**, 5793 (2021).
41. Wattenberg, B. W. The long and the short of ceramides. *J. Biol. Chem.* **293**, 9922–9923 (2018).
42. Wang, J. et al. EMP1 regulates cell proliferation, migration, and stemness in gliomas through PI3K-AKT signaling and CD44. *J. Cell Biochem.* **120**, 17142–17150 (2019).

43. Zeng, Y. et al. SMYD3 drives the proliferation in gastric cancer cells via reducing EMP1 expression in an H4K20me3-dependent manner. *Cell Death Dis.* **14**, 386 (2023).
44. Liu, Y., Ding, Y., Nie, Y. & Yang, M. EMP1 promotes the proliferation and invasion of ovarian cancer cells through activating the MAPK Pathway. *Onco. Targets Ther.* **13**, 2047–2055 (2020).
45. Kovuru, N. et al. Deregulated protein homeostasis constrains fetal hematopoietic stem cell pool expansion in Fanconi anemia. *Nat. Commun.* **15**, 1852 (2024).
46. Chua, B. A. et al. Hematopoietic stem cells preferentially traffic misfolded proteins to aggresomes and depend on aggrephagy to maintain protein homeostasis. *Cell Stem Cell* **30**, 460–472.e466 (2023).
47. Signer, R. A., Magee, J. A., Salic, A. & Morrison, S. J. Haematopoietic stem cells require a highly regulated protein synthesis rate. *Nature* **509**, 49–54 (2014).
48. Shi, Z. et al. C/EBP homologous protein deficiency enhances hematopoietic stem cell function via reducing ATF3/ROS-induced cell apoptosis. *Aging Cell* **20**, e13382 (2021).
49. Liu, B. et al. EVA1A regulates hematopoietic stem cell regeneration via ER-mitochondria mediated apoptosis. *Cell Death Dis.* **14**, 71 (2023).
50. Rouault-Pierre, K. et al. HIF-2α protects human hematopoietic stem/progenitors and acute myeloid leukemic cells from apoptosis induced by endoplasmic reticulum stress. *Cell Stem Cell* **13**, 549–563 (2013).
51. Miharada, K., Sigurdsson, V. & Karlsson, S. Dppa5 improves hematopoietic stem cell activity by reducing endoplasmic reticulum stress. *Cell Rep.* **7**, 1381–1392 (2014).
52. Xie, S. Z. et al. Sphingolipid modulation activates proteostasis programs to govern human hematopoietic stem cell self-renewal. *Cell Stem Cell* **25**, 639–653.e637 (2019).
53. York, A. G. et al. IL-10 constrains sphingolipid metabolism to limit inflammation. *Nature* **627**, 628–635 (2024).
54. Imgrund, S. et al. Adult ceramide synthase 2 (CERS2)-deficient mice exhibit myelin sheath defects, cerebellar degeneration, and hepatocarcinomas. *J. Biol. Chem.* **284**, 33549–33560 (2009).
55. McNally, B. D. et al. Long-chain ceramides are cell non-autonomous signals linking lipotoxicity to endoplasmic reticulum stress in skeletal muscle. *Nat. Commun.* **13**, 1748 (2022).
56. Ferreira, N. S. et al. Regulation of very-long acyl chain ceramide synthesis by acyl-CoA-binding protein. *J. Biol. Chem.* **292**, 7588–7597 (2017).
57. Jensen, S. A. et al. Bcl2L13 is a ceramide synthase inhibitor in glioblastoma. *Proc. Natl. Acad. Sci. USA* **111**, 5682–5687 (2014).
58. Rubio-Lara, J. A. et al. Expanding hematopoietic stem cell ex vivo: recent advances and technical considerations. *Exp. Hematol.* **125-126**, 6–15 (2023).
59. Shao, L., Luo, Y. & Zhou, D. Hematopoietic stem cell injury induced by ionizing radiation. *Antioxid. Redox Signal* **20**, 1447–1462 (2014).
60. Luan, H. et al. rhTPO ameliorates radiation-induced long-term hematopoietic stem cell Injury in Mice. Molecules 28, 1953 (2023).
61. Zhou, C. et al. Nynrin preserves hematopoietic stem cell function by inhibiting the mitochondrial permeability transition pore opening. *Cell Stem Cell* **31**, 1359–1375.e1358 (2024).
62. Hu, Y. & Smyth, G. K. ELDA: extreme limiting dilution analysis for comparing depleted and enriched populations in stem cell and other assays. *J. Immunol. Methods* **347**, 70–78 (2009).
63. Chen, Z. et al. Inhibition of DEK restores hematopoietic stem cell function in Fanconi anemia. *J. Exp. Med.* **222**, e20241248 (2025).

Acknowledgements

This work was supported by grants from Chongqing Science Fund for Distinguished Young Scholars (CSTB2022NSCQ-JQX0032), National Natural Science Foundation of China (82170115), CQMU Program for Youth Innovation in Future Medicine (W0156), and Science and Technology Research Program of Chongqing Municipal Education Commission (Grant No. KJQN202400465). Chongqing Postdoctoral Science Foundation (CSTB2023NSCQ-BHX0144 and 2022CQBSHTB1012).

Author contributions

Y.H., Z.C., and J.P.C. conceived the project. L.L. and Y.F.L. performed the biological experiments. Y.L. performed the bioinformatics analysis. L.L., F.W., and P.S.H. established the ER Stress mouse model. Y.F.L., Y.X.X., and X.Y.Z. performed the transplantation assay and genotyping. W.R.W., J.K.F., and J.M.W. collected human samples. Z.C., Y.H., and L.L. wrote the paper. All authors approved the final version of the manuscript.

Competing interests

The authors declare no competing interests.

Additional information

Supplementary information The online version contains supplementary material available at https://doi.org/10.1038/s41467-025-61552-0.

Correspondence and requests for materials should be addressed to Jieping Chen, Zhe Chen or Yu Hou.

Peer review information *Nature Communications* thanks Daisuke Nakada, John Chute, Kefeng Lu, and the other, anonymous, reviewer(s) for their contribution to the peer review of this work. A peer review file is available.